MAX-PLANCK-GESELLSCHAFT
Fritz-Haber-Institut

Masterarbeit

Machine Learning of the Stability of Octet Binaries

erstellt von
Emre Ahmetcik
Matrikel: 337411

Hochschullehrer:	Prof. Dr. Andreas Knorr, TU Berlin
Betreuer:	Prof. Dr. Matthias Scheffler, FHI
	Dr. Luca Ghiringhelli, FHI
	Dr. Christian Carbogno, FHI

Fritz-Haber-Institut der Max-Planck-Gesellschaft
Theory Department
Berlin, September 2016

Contents

Eidestattliche Erklr̈ung

Die selbständige und eigenständige Anfertigung versichert an Eides statt.

Berlin, den December 26, 2016

Unterschrift

Danksagung

I am grateful for any support from my fiancee, family, friends and colleagues. Special thanks go to my supervisors Luca and Christian. Furthermore I would like to thank Matthias for giving me the opportunity to be involved in such an interesting topic.

Abstract

Statistical learning is regarded as the most promising technique to accelerate and systematically facilitate insights into computational material science. This has been recently successfully demonstrated by using compressed-sensing techniques, for instance to predict the relative stability of zincblende versus rocksalt octet binary materials from the properties of their atomic constituents alone (Ghiringhelli *et al.* Phys. Rev. Lett. **114**, 105503 (2015)). For an application in practical materials science, it is however uncertain to which extent these approaches can be generalized, e.g., to predict metastable polymorphs. To clarify this question, we have computed the relative stability of octet binaries for several different (meta-)stable crystal structures. We use recently developed statistical tools that go beyond the method introduced in the 2015 Phys. Rev. Lett., in order to find a single descriptor (a non-linear function of atomic properties) that quantitatively predicts the difference in energy among eight different polymorphs of the same material. We also introduce a new class of descriptors, mapping the geometry of the different structures into a well defined scalar (the reduced Madelung energy), that is shown to improve the predictive ability of the statistical-learning model.

Zusammenfassung

Statistical Learning wird als die vielverspechensde Herangehensweise betrachtet, um systematisch Einsichten in der Materialwisschenschaft zu gewinnen. In der Tat wurde kürzlich unter Beweis gestellt, dass Energiedifferenzen zwischen Rocksalt und Zincblende für sogenannte *binary octet* Materialien ausschliesslich aus Atomeigenschaften vohergesagt werden können (Ghiringhelli *et al.* Phys. Rev. Lett. **114**, 105503 (2015)). Jedoch müssen solche Ansätze für eine breitere Anwendung erforscht werden. In Anlehnung haben wir Energiedifferencen von *binary octet* Materialien für diverse (meta-)stabile Kristallstrukturen berechnet. Neu entwickelte statistische Methoden werden verwendet, die gegenüber denen im Phys. Rev. Lett. (2015) veröffentlichten Techniken, einen Fortschritt bieten, indem sie einen sogenannten Deskriptor (eine nicht-lineare Funktion der Atomeigenschaften) identifizieren, der mehrere Energiedifferenzen gleichzeitig vorhersagen kann. Desweiteren integrieren wie eine neue Klasse an Deskriptoren: Energien (Madelung-Energie), die geometrische Eigenschaften des Kristalls abbilden. Diese tragen zur akkurateren Vorhersage der Energiedifferenzen bei.

1 Introduction

There are about 200 000 materials known to exist, however the basic properties, such as elastic modulus or conductivity, are known for only a few of them. While studying promising materials for different applications (catalysis, thermoelectricity, photovoltaics), the amount of data increases exponentially with time and stored data is not used again. The use of machine learning on this *big data* provides an alternative, efficient way to reach the target. The data is analysed by modern statistical techniques to explore correlations and identify trends and anomalies, such that predictions for new materials can be readily made. The gained insights would facilitate the rational design of advanced materials. However, many challenges remain to be overcome to enable the statistical learning approach to reach its full potential. For progress to be made, two critical aspects are required: (1) the structured storage of big data, being available and easy to read out by scientists (like a reference book); (2) the efficient application of statistical techniques which handle large amounts of data and give reliable predictions of materials properties. The former is already in avail, such as the NOMAD data base [12], being designed and enhanced for the explained purpose. The latter is a young and fast growing field in material science, and trustful machine-learning methods for a broad use still have do be developed and tested.

One significant progress has been recently realized by using compressed-sensing techniques to predict the relative stability of zincblende versus rocksalt octet binary materials from the properties of the atomic constituents alone [10]. The application on octet binary materials, which is a rather well studied field, provides a simple platform to develop and study machine-learning techniques for a practical application in material science. The prediction of the relative stability between rocksalt and zincblende crystals structure for the same material is only one example of perhaps the most fundamental and important challenge in materials science, i.e., the prediction of the ground-state and metastable crystal structures of a material, given its composition.

Trends in the relative stability of these AB compounds have been analysed long ago, and correlations to physical parameters (coordinates) have been found to classify the materials in 2-dimensional structure maps, separating the comnpounds with respect to (meta-)stable or ground state structures. Coordinates as Mooser and Pearson's ($\mathit{\Delta}\chi$,$\overline{n}$) [11] with Pauling's electronegativity scale $\mathit{\Delta}\chi$ vs. the average principal quantum number $\overline{n} = \frac{1}{2}(n(A) + n(B))$ or Phillips and Van Vechten's (E_h, C) [13, 14, 15] with the average covalent energy gap E_h and the average ionic energy gap C have proven successful. A further pair (r_σ,r_π) [16] based on orbitally dependent radii r_σ and r_π was presented by St.

John and Bloch.

By using compressed sensing techniques, Ghiringhelli et al. [10] introduced a scheme, to overcome the cumbersome trial-and-error search for such coordinates (*descriptors*). The authors demonstrated how the most important descriptors can be determined out of several thousand candidate features, where the candidate features consist of atomic input parameters (*primary features*) such as orbital radii and atomic Kohn-Sham energy levels. The work goes one step beyond only classifying the octet binaries, predicting also the gauge of their relative stability (energy differences). However, the underlying technique is limited to feature spaces of few thousands features, and thus restricted to rather simple non-linear functions of a small number of physical input parameters.

In this thesis, a recently developed scheme is presented, which discovers the most important features out of more than 10^{10} candidates to describe the relative (meta-)stability of octet binary compounds. The developed scheme is applied to predict the energy differences between eight crystal structures of the 82 octet binary compounds. The eight crystal structures of the octet binaries examined are: zincblende, rocksalt, CsCl, NiAs, NaTi, CoSn, NbP, CrB. The crystal structures had their energies predicted using density-functional theory within the local density approximation (LDA). The structures NiAs, CoSn, NbP and CrB have proven to be more complex systems than the original cubic structures, leading to multiple minima and hence the necessity for extensive scans with a careful and critical analysis. In this work, the interest is laid on *advanced* descriptors providing the opportunity, that one descriptor can predict several energy differences at the same time. Moreover, non-linear functions of higher complexity are used and the number of primary features is extended, including the atomic number, valence-electron numbers and also non-atomic parameters as dimers distances and the Madelung energy. Due to logical and physical restriction to be applied to the possible candidate primary features, i.e., that their determination must involve much less intensive calculations than those needed for the energy differences, the Madelung energy, depending on the geometry of the crystal, is included in an indirect way by a two-step procedure, that involves first the prediction of the crystal geometry from atomic features.
The main result is the identification of a procedure for finding a low dimensional descriptor and a model, that is able to quantitatively predict the relative stability (the difference in energy) between the eight selected crystal structures for each of the 82 octet-binary material, with a prediction (absolute) error that is on average smaller than 0.1 eV per atom.

The present thesis is divided into six chapters. Chapter 2 briefly summarizes the concepts of electronic-structure theory. In chapter 3 an introduction to the used statistical methods is given. This involves motivations and mathematical basics, providing detailed and descriptive insights. The details about the electronic structure calculations is presented in Chapter

4, giving a concise description of the techniques to find the equilibrium properties of the materials. Afterwards, in Chapter 5 the target to predict energy differences is formulated and put in an statistical concept, followed by the results. Chapter 6 summarizes and concludes the work.

2 Theoretical backround

2.1 The many-electron problem

In order to understand the physics of solids and molecular systems, we consider here the time-independent Schrödinger equation

$$\hat{H}\mathit{\Psi} = E\mathit{\Psi} \tag{2.1}$$

for a set of interacting atoms, consisting of N_{el} electrons and N_{nuc} nuclei. We may write the non-relativistic Hamiltonian as a sum [3]

$$\hat{H} = \hat{T}_{\mathrm{el}} + \hat{T}_{\mathrm{nuc}} + \hat{V}_{\text{el-el}} + \hat{V}_{\text{el-nuc}} + \hat{V}_{\text{nuc-nuc}} \tag{2.2}$$

of the kinetic energy operator of the electrons

$$\hat{T}_{\mathrm{el}} = -\frac{1}{2}\sum_{i}^{N_{\mathrm{el}}} \Delta_i, \tag{2.3}$$

the kinetic energy operator of the nuclei

$$\hat{T}_{\mathrm{nuc}} = -\frac{1}{2}\sum_{i}^{N_{\mathrm{nuc}}} \frac{\Delta_I}{M_I}, \tag{2.4}$$

the electron-electron interaction operator

$$\hat{V}_{\text{el-el}} = \frac{1}{2}\sum_{i}^{N_{\mathrm{el}}}\sum_{j\neq i}^{N_{\mathrm{el}}} \frac{1}{|\boldsymbol{r}_i - \boldsymbol{r}_j|}, \tag{2.5}$$

the electron-nuclear interaction operator

$$\hat{V}_{\text{el-nuc}} = -\frac{1}{2}\sum_{i}^{N_{\mathrm{el}}}\sum_{I}^{N_{\mathrm{nuc}}} \frac{Z_I}{|\boldsymbol{r}_i - \boldsymbol{R}_I|}, \tag{2.6}$$

and the nuclear-nuclear interaction operator

$$\hat{V}_{\text{nuc-nuc}} = \frac{1}{2}\sum_{I}^{N_{\mathrm{nuc}}}\sum_{J\neq I}^{N_{\mathrm{nuc}}} \frac{Z_I Z_J}{|\boldsymbol{R}_I - \boldsymbol{R}_J|}. \tag{2.7}$$

Here atomic units are used. The electronic and nuclear coordinates are given by $\boldsymbol{r}_i$ and $\boldsymbol{R}_I$, the Laplacian by Δ.
The ratio $\frac{m_i}{M_I} < 10^{-4}$ leads to the fact, that the nuclei move much slower than the electrons, which allows us to to treat, in an (the Born-Oppenheimer) approximation, the electrons as following the movements of the nuclei adiabatically, which allows us to factorize the wavefunction into an electronic and a nuclear part:

$$\Psi = \Psi_{\mathrm{el}}(\boldsymbol{r}_i, \{\boldsymbol{R}_I\})\Psi_{\mathrm{nuc}}(\boldsymbol{R}_I). \tag{2.8}$$

Here Ψ_{el} depends only parametrically on the nuclear coordinates $\boldsymbol{R}_I$ as highlighted by the brackets $\{\}$. As a result 2.1 can be decoupled into an electronic equation

$$\hat{H}_{\mathrm{el}}\Psi_{\mathrm{el}} = E_{\mathrm{el}}\Psi_{\mathrm{el}} \tag{2.9}$$

with

$$\hat{H}_{\mathrm{el}} = \hat{T}_{\mathrm{el}} + \hat{V}_{\text{el-el}} + \hat{V}_{\text{el-nuc}} \tag{2.10}$$

and into an nuclear equation

$$\left[-\frac{1}{2}\sum_{i}^{N_{\mathrm{nuc}}}\frac{\Delta_I}{M_I} + \hat{V}_{\text{nuc-nuc}} + E_{\mathrm{el}}(\{\boldsymbol{R}_I\})\right]\Psi_{\mathrm{nuc}} = E_{\mathrm{nuc}}\Psi_{\mathrm{nuc}}. \tag{2.11}$$

2.2 Density-functional theory and Hohenberg-Kohn Theorems

The electronic equation 2.9 depends on the function Ψ_{el} with $3N_{\mathrm{el}}$ variables. Density-functional theory is based on the fact, that the energy of the electrons can be written as a functional of the electron density $n(\boldsymbol{r})$ and the ground state energy is obtained from the minimum of the the functional via variation of $n(\boldsymbol{r})$. As a result, the complexity of the problem is reduced, since the electron density

$$n(\boldsymbol{r}) = N_{\mathrm{el}}\int ... \int |\Psi_{\mathrm{el}}(\boldsymbol{r}, \boldsymbol{r}_2, ..., \boldsymbol{r}_{N_{\mathrm{el}}})|^2 \,\mathrm{d}\boldsymbol{r}_{2 ... N_{\mathrm{el}}} \tag{2.12}$$

depends on only 3 variables. The theory is build on the two Hohenberg-Kohn theorems [4]

First Hohenberg-Kohn theorem: *For any system of interacting particles in an external potential, the external potential is determined up to a constant by the ground state electron density.*

Second Hohenberg-Kohn theorem: *A universal functional $E[n]$ of the electron density existsts. The minimum of the functional via variation of $n(\boldsymbol{r})$ is the ground state energy at the ground state electron density.*

The energy functional is defined as

$$E[n] = F[n] + \int \nu_{\text{ext}}(\boldsymbol{r}) n(\boldsymbol{r}) \mathrm{d}\boldsymbol{r} \tag{2.13}$$

with the external potential $\nu_{\text{ext}}(\boldsymbol{r})$ and the universal functional

$$F[n] = \langle g | \hat{T}_{\text{el}} + \hat{V}_{\text{el-el}} | g \rangle = T_{\text{el}}[n] + E_{\text{el-el}}[n]. \tag{2.14}$$

Here, $\langle \cdot | \cdot \rangle$ denotes the usual bra-ket notation and $|g\rangle$ the ground state.

2.3 Kohn-Sham equations

Formally the expression 2.14 is exact, however the analytical form of the functional $F[n]$ remains unknown, also no satisfying direct approximations exist [5]. A way to solve this problem by reintroducing individual electronic states, was presented by Kohn and Sham. The idea behind the approach of Kohn and Sham [6] is that we study a system of non-interacting electrons in an auxiliary potential V_{aux}. This system is constructed such that it has the same ground-state density as the interacting system and thus, by the Hohenberg-Kohn theorems, the same ground-state energy. This non-interacting system is described by the Schrödinger equation

$$(-\frac{1}{2}\Delta + v_{\text{aux}})\phi_i(\boldsymbol{r}) = \epsilon_i \phi_i(\boldsymbol{r}). \tag{2.15}$$

It has the electron density

$$n = \sum_i^{N_{el}} \int |\phi_i(\boldsymbol{r})|^2 d\mathbf{r}. \tag{2.16}$$

In this spirit, the energy $E[n]$ of the interacting system is rewritten

$$E[n] = \bar{T}_{\text{s}}[n] + E_{\text{H}}[n] + \int \nu_{\text{ext}}(\boldsymbol{r}) n(\boldsymbol{r}) \mathrm{d}\boldsymbol{r} + E_{\text{xc}}[n] \tag{2.17}$$

with the kinetic energy $\bar{T}_s[n]$ of the non interacting electron system , the exchange-correlation functional

$$E_{\text{xc}}[n] = F[n] - \bar{T}_{\text{s}}[n] - E_{\text{H}}[n], \tag{2.18}$$

and the the Hartree energy

$$E_{\text{H}} = \frac{1}{2} \int\int \frac{n(\boldsymbol{r}) n(\boldsymbol{r'})}{|\boldsymbol{r} - \boldsymbol{r'}|}, \mathrm{d}\boldsymbol{r}\mathrm{d}\boldsymbol{r'}. \tag{2.19}$$

This provides a mapping between the non interacting auxiliary system and the interacting system. The variational minimum of Eq. (2.17) is given by

$$\frac{\delta \bar{T}_{\text{s}}[n]}{\delta n(\boldsymbol{r})} + \frac{\delta E_{\text{H}}[n]}{\delta n(\boldsymbol{r})} + \nu_{\text{ext}}(\boldsymbol{r}) + \frac{\delta E_{\text{xc}}[n]}{\delta n(\boldsymbol{r})} - \frac{\delta}{\delta n(\boldsymbol{r})}(\mu \int n(\boldsymbol{r'}) \mathrm{d}\boldsymbol{r'}) = 0 \tag{2.20}$$

$$\frac{\delta \bar{T}_{\mathrm{s}}[n]}{\delta n(\boldsymbol{r})} + \underbrace{\nu_{\mathrm{H}}[n](\boldsymbol{r}) + \nu_{\mathrm{ext}}[n](\boldsymbol{r}) + \nu_{\mathrm{xc}}[n](\boldsymbol{r})}_{V_{\mathrm{aux}}(\boldsymbol{r})} - \mu = 0 \tag{2.21}$$

whereby the Lagrange multiplier μ takes the side condition, that the number of particles

$$N_{\mathrm{el}} = \int n(\boldsymbol{r'})\mathrm{d}\boldsymbol{r'} \tag{2.22}$$

shall be fixed, into account.

To solve Eq. (2.21) we would need to know an expression for the functional $\bar{T}_s[n]$ in terms of the density. Although we do not know an exact expression of $\bar{T}_s[n]$, we can express it in terms of single particle states:

$$T_{\mathrm{s}}[n] = -\frac{1}{2}\sum_{i}^{N_{\mathrm{el}}} \langle \phi_i | \Delta | \phi_i \rangle \,. \tag{2.23}$$

where the orbitals ϕ_i are connected to the density n through

$$\underbrace{\left[-\frac{1}{2}\Delta + v_{\mathrm{aux}}(\boldsymbol{r})\right]}_{h_{\mathrm{KS}}} \phi_i(\boldsymbol{r}) = \epsilon_i \phi_i(\boldsymbol{r}). \tag{2.24}$$

The electron density is obtained by solving the Kohn-Sham equations 2.24 and 2.16 in a self-consistent manner. The energy is determined by

$$E[n] = \sum_{i}^{\mathrm{occ.}} \epsilon_i - E_{\mathrm{H}}[n] - \int \nu_{\mathrm{xc}}(\boldsymbol{r}) n(\boldsymbol{r}) \mathrm{d}\boldsymbol{r} + E_{\mathrm{xc}}[n]. \tag{2.25}$$

2.4 Approximations to the exchange-correlation functional

To obtain the exact ground state energy, the energy functional 2.17 must be known. The only unknown part is the energy-correlation functional, so approximations to it are needed. There exist different approximations with different level of accuracy and computational cost. In the following the concepts behind *local-density approximation*, the *generalized gradient approximation*, and hybrid functionals are introduced.

2.4.1 Local-density approximation

The simplest approximation is the local-density approximation (LDA), in which the electron density is locally approximated by a homogeneous electron gas. The exchange-correlation functional is written

$$E_{\mathrm{xc}}^{\mathrm{LDA}}[n] = \int n(\boldsymbol{r}) \epsilon_{\mathrm{xc}}^{\mathrm{LDA}}(n(\boldsymbol{r})) \mathrm{d}\boldsymbol{r}. \tag{2.26}$$

2.4.2 Generalized gradient approximation

The generalized gradient approximation introduces an explicit dependence on the gradient of the density in the exchange-correlation functional

$$E_{\mathrm{xc}}^{\mathrm{GGA}}[n] = \int n(\boldsymbol{r})\epsilon_{\mathrm{xc}}^{\mathrm{LDA}}(n(\boldsymbol{r}))K_{\mathrm{xc}}(n(\boldsymbol{r}), \nabla n(\boldsymbol{r}))\mathrm{d}\boldsymbol{r}, \tag{2.27}$$

where $K_{\mathrm{xc}}(n(\boldsymbol{r}), \nabla n(\boldsymbol{r}))$ is a factor modifying $\epsilon_{\mathrm{xc}}^{\mathrm{LDA}}(n)$ in dependence of $n(\boldsymbol{r})$ and $\nabla n(\boldsymbol{r}))$. Examples are the PBE[7] or PBEsol[8] functional. Going beyond, in the so-called meta-GGA, also the second derivative of the electron density is considered.

2.4.3 Hybrid functionals

Further improvements are obtained by using hybrid functionals, which reduce the so-called self-interaction error. The exchange functional is given by

$$E_{\mathrm{x}}^{\mathrm{hyb}} = \alpha E_{\mathrm{x}}^{\mathrm{HF}} + (1-\alpha)E_{\mathrm{x}}^{\mathrm{DFA}}, \tag{2.28}$$

with the Hartree-Fock (HF) exchange

$$E_{\mathrm{x}}^{\mathrm{HF}} = -\frac{1}{2}\sum_{i,j}^{\mathrm{occ.}}\int\int \frac{\phi_i^*(\boldsymbol{r})\phi_j(\boldsymbol{r})\phi_j^*(\boldsymbol{r'})\phi_i(\boldsymbol{r'})}{|\boldsymbol{r}-\boldsymbol{r'}|}, \mathrm{d}\boldsymbol{r}\mathrm{d}\boldsymbol{r'} \tag{2.29}$$

and the parameter $\alpha \in [0,1]$, determining the weight of the HF contribution to a Density-Functional approximation (DFA) exchange.

2.5 Solving the Kohn-Sham equations

We would like to solve the Kohn-Sham equations in an efficient implementation, now. A truncated expansion

$$\phi_i = \sum_j c_{ij}\varphi_j \tag{2.30}$$

is used, where c_{ij} are expansion coefficients and φ_j are basis functions. Thus the Kohn-Sham equations translate into a eigenvalue problem

$$\sum_j h_{nj}c_{ji} = \epsilon_i \sum_j A_{nj}c_{ji} \tag{2.31}$$

Here h_{nj} are the matrix elements of the Kohn-Sham hamiltonian h_{KS}

$$h_{nj} = \int \varphi_n^*(\boldsymbol{r})h_{\mathrm{KS}}\varphi_j(\boldsymbol{r})d\boldsymbol{r}, \tag{2.32}$$

and the A_{nj} are the components of the overlap matrix

$$A_{nj} = \int \varphi_n^*(\boldsymbol{r})\varphi_j(\boldsymbol{r})d\boldsymbol{r}. \tag{2.33}$$

In this work, the code FHI-aims [9] is used, which is an all-electron, full potential code utilizing numeric atom-centered basis functions

$$\varphi_i(\boldsymbol{r}) = \frac{u_{nl}(\boldsymbol{r} - \boldsymbol{R}_{\text{nuc}})}{r} Y_{lm}(\Theta, \Phi). \tag{2.34}$$

The $Y_{lm}(\theta, \phi)$ are spherical harmonics and the $u_{nl}(\boldsymbol{r} - \boldsymbol{R}_{\text{nuc}})$ are numerically defined radial functions, centered at the considered nucleus.

2.6 Periodic boundary conditions

To describe materials with periodically arranged constituents in an efficient way, a unit cell for the considered system is defined, being spanned by three lattice vector a_1, a_2 and a_3. Additional we define the basis, as the positions of the atoms in the unit cell. The unit cell with its basis is chosen, such that, the periodic system can be described by infinitely repeating the unit cell. To map to each unit cell a translation vector $\boldsymbol{T}(\boldsymbol{n}) = \boldsymbol{A}\boldsymbol{n}$ is used with a vector $\boldsymbol{n} = (n_1, n_2, n_3)$, where $n_i \in \mathbb{Z}$ and $\boldsymbol{A} = (\boldsymbol{a_1}, \boldsymbol{a_2}, \boldsymbol{a_3})$.
The periodicity imposes restrictions on the form of the orbitals. The so called Bloch theorem states, that the orbitals can be written

$$\phi_i^{(\boldsymbol{k})} = e^{i\boldsymbol{k}\boldsymbol{r}} u_i^{(\boldsymbol{k})}(\boldsymbol{r}) \tag{2.35}$$

with

$$u_i^{(\boldsymbol{k})}(\boldsymbol{r}) = u_i^{(\boldsymbol{k})}(\boldsymbol{r} + \boldsymbol{T}(\boldsymbol{n})). \tag{2.36}$$

In FHI-aims this is accounted for by using Bloch-like basisfunction

$$\Theta(\boldsymbol{r}, \boldsymbol{k}) = \sum_n e^{i\boldsymbol{k}\cdot T(\boldsymbol{n})} \varphi(\boldsymbol{r} - \boldsymbol{R}_{nuc} + \boldsymbol{T}(\boldsymbol{n})). \tag{2.37}$$

As a result the KS Hamiltonian h_{KS} and the KS states $\phi_i(\boldsymbol{r})$ become $\boldsymbol{k}$ dependant. In practice a finite number of k points is considered, leading to the need of testing the convergence of the property of interest with respect to the density of the *k-grid.*

2.7 Madelung energy

The Madelung energy denotes the electrostatic energy of as point charges approximated ions in a crystal. We define the Madelung energy per ion pair on the side of ion i:

$$E_{\text{mad},i} = -\frac{z^2 e^2}{4\pi\epsilon r_0} M_i. \tag{2.38}$$

Here z is the number of charges of an ion, e the electric charge and ϵ Coulomb's constant. The Madelung constant

$$M = \sum_j \frac{\pm 1}{r_{ij}/r_0} \tag{2.39}$$

is a sum over the ions with positive and negative charges in the crystal, where r_{ij} denotes the distance between atom i and atom j normalized by a distance r_0, e.g. the nearest neighbour distance. Moreover we introduce the *reduced* Madelung energy, in which the charges are neglected:

$$E_{\mathrm{mad},i} = -\frac{e^2}{4\pi\epsilon r_0} M_i. \tag{2.40}$$

3 Statistical-learning background

In this study, a recently developed statistical learning scheme [2] is applied to enable construction of a sparse (low-dimensional) descriptor that accurately predicts materials properties of interest. The descriptor is selected out of a feature space of 10^{10} candidates to ensure that an accurate model can constructed. The aim of the used methods is to find linear models $f(\{\boldsymbol{d}_i\})$ (or linear combinations) of only a few vectors of a huge set of m input vectors $\boldsymbol{d}_i \in \mathbb{R}^m$, approximating a target vector $\boldsymbol{P} \in \mathbb{R}^n$, as good as possible.
We call $\boldsymbol{P}$ the *property*, consisting of a chosen physical property of n materials, to be predicted. The vectors $\boldsymbol{d}_i$ are called *descriptors*, where each entry is a function of some physical input parameters, which map to a material. In this work, we define *non-linear* functions of the input parameters, so that the resulting model is a linear combination of non-linear functions of the input parameters. A *descriptor matrix* $\boldsymbol{D} \in \mathbb{R}^{n\times m+1}$ is constructed out of the m available descriptors, as columns, with an additional column full of ones [1]. The mapping $f : \mathbb{R}^{m+1} \rightarrow \mathbb{R}^n$ is defined by

$$f(\boldsymbol{c}) = \boldsymbol{D}\boldsymbol{c}, \tag{3.1}$$

where $\boldsymbol{c}$ is the coefficient vector. The coefficient corresponding to the vector full of ones is called *bias* and will be included in all our solutions. The number of non-zero coefficients is denoted by

$$\|\boldsymbol{c}\|_0 = |\{j, c_j \neq 0\}|. \tag{3.2}$$

Here, the symbol $|\cdot|$ denotes the cardinality of a set, e.g. the number of elements in the set. A vector $\boldsymbol{c}$ with $\|\boldsymbol{c}\|_0 \leq k$ is called k-sparse. If $\|\boldsymbol{c}^*\|_0 = k$, we call the model $f(\boldsymbol{c}^*)$ a $(k-1)$-*dimensional descriptor*. Since the bias is included in all our models, a 0-dimensional descriptor is a vector full of the bias. The target is to find a low dimensional descriptor[2], which minimizes the euclidean distance between $\boldsymbol{P}$ and $\boldsymbol{D}\boldsymbol{c}$. This kind of constraining $\boldsymbol{c}$, is called ℓ_0-*regularization* and written

$$\underset{\boldsymbol{c}\in\mathbb{R}^m}{\arg\min}\{\|\boldsymbol{P} - \boldsymbol{D}\boldsymbol{c}\|_2^2 + \lambda\|\boldsymbol{c}\|_0\}. \tag{3.3}$$

---

[1] In general, linear functions include an absolute term c_0, e.g. $f(x_1, ..., x_k) = c_0 + c_1x_1 + ...c_kx_k$, where $\{c_1, ...c_k\}$ are constants and $\{x_1, ..., x_k\}$ variables.

[2] In this work we focus on values $\|\boldsymbol{c}\|_0 \leq 8$

Here, $\| \cdot \|_2$ denotes the euclidean norm (ℓ_2-*norm*). In Eq. 3.3 a compromise between a small ℓ_2-*norm* and a sparse solution is sought[3]. The sparsity is tuned by the regularization parameter $\lambda \in \mathbb{R}_0^+$. The significant drawback of solving this problem is, that it becomes computationally infeasible with increasing sparsity and size of the feature space. The problem is called *NP-hard* [28]. In this context, it suffices to say that there is essentially no better algorithm to solve *exactly* Eq. 3.3 than enumerating all possible solutions (combinations of non-zero coefficients) for the given level of sparsity and select the one with lowest ℓ_2-norm. There are several methods approximating the l_0-problem, such as ℓ_1-regularization as a convex relaxation of 3.3 or greedy algorithms. In this work, different methods are considered, each with its advantages, and combined to a powerful scheme called the ℓ_1-ℓ_0 method [2]. Each of them is used to reduce the feature space size by filtering the *important* descriptors and is applied on a different level of size. They are introduced in the following sections.

3.1 Standardization of the descriptors

When applying ℓ_1-regularization and matching pursuit, it is crucial that the descriptors $\boldsymbol{d}_i$ are comparable, i.e., that their ℓ_2 norms do not affect their contribution. Thus, the $\boldsymbol{d}_i$ are *standardized.* First, each $\boldsymbol{d}_i$ is centered to have mean μ_i=0, to cancel its influence on the bias. The bias of a closest model to $\boldsymbol{P}$ is then given by the mean of $\boldsymbol{P}$ and can be ignored in the minimization problem. Second, each centered $\boldsymbol{d}_i$ is scaled to have same ℓ_2-norm by dividing by the standard deviation σ_i of the not centered $\boldsymbol{d}_i$:

$$\tilde{\boldsymbol{d}}_i = \frac{1}{\sigma_i}(\boldsymbol{d}_i - \boldsymbol{\mu}_i). \tag{3.4}$$

Here, $\boldsymbol{\mu}_i$ is a vector full of μ_i. Note, that if a $\boldsymbol{d}_i \in \mathbb{R}^n$, then $\|\tilde{\boldsymbol{d}}_i\|_2 = \sqrt{n}$. To compare two descriptors $\boldsymbol{d}_i$ and $\boldsymbol{d}_j$ we define the *correlation* (Pearson's correlation)

$$\mathrm{cor}(\boldsymbol{d}_i, \boldsymbol{d}_j) = \frac{\langle \tilde{\boldsymbol{d}}_i, \tilde{\boldsymbol{d}}_j \rangle}{\|\tilde{\boldsymbol{d}}_i\|_2 \|\tilde{\boldsymbol{d}}_j\|_2}, \tag{3.5}$$

where $\langle \cdot,\cdot \rangle$ denotes the dot product. If two standardized $\tilde{\boldsymbol{d}}_i$ and $\tilde{\boldsymbol{d}}_j$ are parallel, their correlation $\mathrm{cor}(\tilde{\boldsymbol{d}}_i, \tilde{\boldsymbol{d}}_j) = 1$

---

[3] The way 3.3 is written, it is assumed that all the columns of $\boldsymbol{D}$ are centered, since the bias should not be effected by the ℓ_0-penalty. A centered column is $\boldsymbol{d}_i - \boldsymbol{\mu}_i$, where $\boldsymbol{\mu}_i$ is a vector full of the mean μ_i of the entries of $\boldsymbol{d}_i$. With centered columns the influence of each column on the bias is cancelled. Thus the bias is not needed in the minimization.

3.2 Least-squares solution

Our scheme (presented in Sec. 3.7) is based on a stepwise technique which filters the most promising descriptors for a sparse linear model in the first steps. With the selected descriptors the coefficients have to be determined, such that $\|\boldsymbol{P} - \boldsymbol{Dc}\|_2$ is minimized, e.g

$$\underset{\boldsymbol{c}\in\mathbb{R}^{k+1}}{\arg\min} \|\boldsymbol{P} - \boldsymbol{Dc}\|_2^2. \tag{3.6}$$

Now $\boldsymbol{c} \in \mathbb{R}^{k+1}$ and $\boldsymbol{D} \in \mathbb{R}^{n\times k+1}$, with k filtered descriptors. The solution to this problem is called *least-squares solution.*

The textbook definitions 1 - 4 are reminded for clarity to define the terms *direct sum, orthogonal complement,* and *orthogonal projection.* Similarly, the textbook theorems 1 to 3 remind what a least-square solution is.

Definition 1 *A vector space V is called the **direct sum** of two subspaces U and W, written $V = U \bigoplus W$, if $V = \{\boldsymbol{u} + \boldsymbol{w} : \boldsymbol{u} \in U, \boldsymbol{w} \in W\}$ and $U \cap W = \{\boldsymbol{0}\}$*

Definition 2 *Let U be subspace of an inner product space V. Then the **orthogonal complement** of U is denoted by $U^\perp = \{\boldsymbol{v} \in V : \langle \boldsymbol{v}, \boldsymbol{u}\rangle = 0, \forall \boldsymbol{u} \in U\}$.*

Definition 3 *Let U and W be subspaces of a vector space V. A linear transformation $T : V \mapsto V$ is called the **projection** of V onto the subspace U along W, if $V = U \bigoplus W$ and $T(\boldsymbol{y}) = \boldsymbol{u}$ for $\boldsymbol{y} = \boldsymbol{u} + \boldsymbol{w} \in U \bigoplus W$*

Definition 4 *Let V be an inner product space, and let U be a subspace of V so that $V = U \bigoplus U^\perp$. Then the projection of V onto U along $U^\perp$ is called the **orthogonal projection** of V onto U, denoted Proj_U. For $\boldsymbol{y} \in V$, the component vector $\mathrm{Proj}_U(\boldsymbol{y}) \in U$ is called **orthogonal projection** of $\boldsymbol{y}$ into U.*

Theorem 1 *Let U be a subspace of an inner product space V, and let $\{\boldsymbol{u}_1, \boldsymbol{u}_2, ..., \boldsymbol{u}_n\}$ be an orthonormal basis for U. Then, for any $\boldsymbol{y} \in V$, the orthogonal projection $\mathrm{Proj}_U(\boldsymbol{y})$ of $\boldsymbol{y}$ into U is*

$$\mathrm{Proj}_U(\boldsymbol{y}) = \langle \boldsymbol{y}, \boldsymbol{u}_1\rangle \boldsymbol{u}_1 + \langle \boldsymbol{y}, \boldsymbol{u}_2\rangle \boldsymbol{u}_2 + ... + \langle \boldsymbol{y}, \boldsymbol{u}_n\rangle \boldsymbol{u}_n. \tag{3.7}$$

Theorem 2 *Let U be a subspace of an inner product space V, and let $\boldsymbol{y} \in V$. Then, the orthogonal projection Proj_U of $\boldsymbol{y}$ satisfies*

$$\|\boldsymbol{y} - \mathrm{Proj}_U(\boldsymbol{y})\|_2 \leq \|\boldsymbol{y} - \boldsymbol{x}\|_2 \tag{3.8}$$

for all $\boldsymbol{x} \in U$. The equality holds if and only if $\boldsymbol{x} = \mathrm{Proj}_U(\boldsymbol{y})$.

Let us now consider the linear system

$$\boldsymbol{P} = \boldsymbol{D}\boldsymbol{c} \tag{3.9}$$

with $\boldsymbol{P} \in \mathbb{R}^n$, $\boldsymbol{D} \in \mathbb{R}^{n \times m}$ and $\boldsymbol{c} \in \mathbb{R}^m$. This system has at least one solution if and only if $\boldsymbol{P}$ belongs to the **column space** $\mathcal{C}(\boldsymbol{D}) = \{\boldsymbol{D}\boldsymbol{c} \in \mathbb{R}^n : \boldsymbol{c} \in \mathbb{R}^m\}$. Now let $\boldsymbol{P} \notin \mathcal{C}(\boldsymbol{D})$. Then we would like to have a solution $\boldsymbol{c}^*$, such that $\boldsymbol{D}\boldsymbol{c}^*$ is as *close* as possible to $\boldsymbol{P}$, e.g.

$$\boldsymbol{c}^* = \operatorname*{arg\,min}_{\boldsymbol{c} \in \mathbb{R}^m} \|\boldsymbol{P} - \boldsymbol{D}\boldsymbol{c}\|_2. \tag{3.10}$$

$\boldsymbol{c}^*$ is called a **least square solution**. From **Theorem 2**, we know, that $\boldsymbol{D}\boldsymbol{c}^*$ is the orthogonal projection of $\boldsymbol{P}$ into $\mathcal{C}(\boldsymbol{D})$. To find this projection the following theorem is used.

Theorem 3 *Let the columns of* $\boldsymbol{D}$ *be linearly independent. Then*

$$\mathrm{Proj}_{\mathcal{C}(\boldsymbol{D})}(\boldsymbol{P}) = \boldsymbol{D}(\boldsymbol{D}^T\boldsymbol{D})^{-1}\boldsymbol{D}^T\boldsymbol{P}. \tag{3.11}$$

To evaluate the performance of a given model $\boldsymbol{D}\boldsymbol{c}^*$, the *mean-square error*

$$\mathrm{MSE} = \frac{1}{n}\|\boldsymbol{P} - \boldsymbol{D}\boldsymbol{c}^*\|_2^2 \tag{3.12}$$

is defined, where n is the dimension of $\boldsymbol{P}$. In the case of this work, n is the number of Materials. In all the results, rather the *root-mean-square error* RMSE $= \sqrt{MSE}$ is reported, as a measurement with the same unit as the predicted quantity. To maximum absolute error (MaxAE) denotes the entry of the vector $\boldsymbol{P} - \boldsymbol{D}\boldsymbol{c}^*$ with the highest absolute value.

3.3 ℓ_0-regularization

The ℓ_0-method will be used as a last step of the used scheme (see Sec. 3.7), for a reduced feature space size below 100. The way of solving 3.3 for a given $\boldsymbol{P}$ and $\boldsymbol{D}$ is explained in the following.

1. Choose a number k for the dimension of the descriptor.
2. Calculate the least square solution $\boldsymbol{c}^*$ for all possible k-dimensional descriptors. This defines a *model* $f(\boldsymbol{c}^*)$ for each k-dimensional descriptor.
3. Choose the model with the lowest MSE.

We go through this procedure for a set of k values, not higher than $k = 7$. The different dimensional descriptors are all considered and compared.

3.4 ℓ_1-regularization

A convex re-formulation of the ℓ_0-regularization is given by the LASSO (Least Absolute Shrinkage and Selection Operator)[26], in which the ℓ_0-norm is replaced by the ℓ_1 norm

$$\|\boldsymbol{c}\|_1 \ = \sum_i |c_i|. \tag{3.13}$$

The problem is denoted by

$$\arg\min_{\boldsymbol{c}\in\mathbb{R}^m}\{\|\boldsymbol{P}-\boldsymbol{D}\boldsymbol{c}\|_2^2+\lambda\|\boldsymbol{c}\|_1\}. \tag{3.14}$$

Now a compromise between a small euclidean distance and a small $\|\boldsymbol{c}\|_1$ is sought. This leads to sparse solutions, which lie on the edges of the ℓ_1-ball $B_\tau = \{\boldsymbol{c}\in\mathbb{R}^m : \|\boldsymbol{c}\|_1 \leq \tau\}$, see Fig. 3.1. With decreasing λ, τ increases, such that the solutions become less sparse. For $\lambda \to 0$ the solution converges to the least square solution. Note, that we use the LASSO with standardized matrices $\boldsymbol{D}$. In this way, the ℓ_2-norm of a column does not affect bias its contribution to the model. If the columns did not have all same ℓ_2-norm, columns with relatively small ℓ_2-norm would need higher coefficients to be comparable with other columns, but since high coefficients are penalized, these *small*-ℓ_2-norm columns could be disadvantaged.

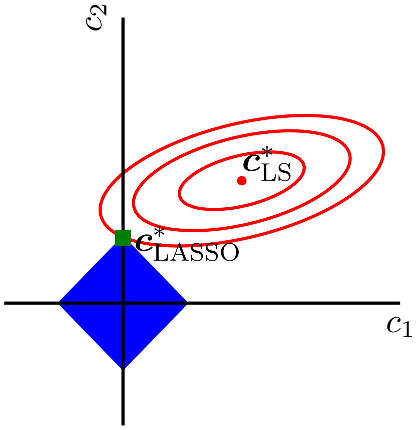

Figure 3.1: A schematic depicting the LASSO estimation of coefficients c_1 and c_2.. The red ellipses are the contours of the LS error function. The blue area is the constraint region $\|\boldsymbol{c}\|_1 \leq \tau$.

3.4.1 Multi-task LASSO

In this work, we are also interested in finding descriptors, which are the same for different property vectors $\boldsymbol{P}_j$. The difference between the models f_j lies in the values of the non-zero coefficients, e.g. the *weights* on the descriptors. We construct a property matrix $\boldsymbol{B} \in \mathbb{R}^{n\times q}$

out of q different properties $\boldsymbol{P}_j \in \mathbb{R}^n$, and analogously a coefficient matrix $\boldsymbol{C} \in \mathbb{R}^{m\times q}$. Our target is achieved by the multi-task LASSO

$$\operatorname*{arg\,min}_{\boldsymbol{C}\in\mathbb{R}^{m\times q}}\{\|\boldsymbol{B}-\boldsymbol{D}\boldsymbol{C}\|_{\mathrm{F}}^2+\lambda\sum_{r=1}^{m}\sqrt{\sum_{s=1}^{q}C_{rs}^2}, \tag{3.15}$$

where the *Frobenius norm* of a matrix $\boldsymbol{A} \in \mathbb{R}^{n\times m}$ is denoted by

$$\|\boldsymbol{A}\|_{\mathrm{F}} = \sqrt{\sum_{i=1}^{n}\sum_{j=1}^{m}A_{ij}^2}. \tag{3.16}$$

The solutions of the multi-task LASSO, are "sparse" matrices $\boldsymbol{C}$, in the sense, that only a few rows of $\boldsymbol{C}$ are not full of zeros. For $q = 1$, the multi-task LASSO is the same as LASSO.

3.4.2 Compressed sensing

We now consider the target, to recover the sparsest $\boldsymbol{c}$ from $\boldsymbol{P} = \boldsymbol{D}\boldsymbol{c}$. In the theory of compressed sensing (CS), it is studied under which conditions the solutions of

$$\operatorname*{arg\,min}_{\boldsymbol{c}\in\mathbb{R}^{m}}\|\boldsymbol{c}\|_0 \qquad \text{subject to } \boldsymbol{P}=\boldsymbol{D}\boldsymbol{c}, \tag{3.17}$$

and

$$\operatorname*{arg\,min}_{\boldsymbol{c}\in\mathbb{R}^{m}}\|\boldsymbol{c}\|_1 \qquad \text{subject to } \boldsymbol{P}=\boldsymbol{D}\boldsymbol{c}, \tag{3.18}$$

coincide. An important result is given in the following definition and result, taken from Ref. [30].

Definition 5 *The matrix $\boldsymbol{D} \in \mathbb{R}^{n\times m}$ is said to have the Null Space Property (NSP) of order $k \in M = \{1, ..., m\}$ if*

$$\sum_{j\in K}|v_j| < \sum_{j\notin K}|v_j| \tag{3.19}$$

for all $\boldsymbol{v} \in \ker\boldsymbol{D} \setminus \{\boldsymbol{0}\}$ and all $K \subset M$ with $|K| \leq k$.

Theorem 4 *Let $\boldsymbol{D} \in \mathbb{R}^{n\times m}$ and let $k \in \{1, ..., m\}$. Then every k-sparse vector $\boldsymbol{c} \in \mathbb{R}^m$ is the unique solution of 3.14, with $\boldsymbol{P} = \boldsymbol{D}\boldsymbol{c}$ if and only if $\boldsymbol{D}$ satisfies the NSP of order k.*

Unfortunately it is not easy, to check, if a matrix has the NSP. Nevertheless it is known, that there exists a constant C such that whenever

$$n > Ck\ln(m), \tag{3.20}$$

there exists a $\boldsymbol{D} \in \mathbb{R}^{n\times m}$ with NSP of order k. If $\boldsymbol{D}$ is a random matrix, it will satisfy the NSP with high probability.

3.5 The ℓ_1-ℓ_0 method

In the recently demonstrated ℓ_1-ℓ_0 method [10], the ℓ_1-regularization is used to reduce the size of the feature space to a small number N_{ℓ_1}(in our cases $N_{\ell_1} < 100$), and apply the ℓ_0-regularization with a matrix $\boldsymbol{D} \in \mathbb{R}^{n\times N_{\ell_1}+1}$. For low N_{ℓ_1} and low sparsity, the ℓ_0-step is computational feasible. The method is described in the following

1. Build a sequence of 120 λ-values on a log scale, with $\lambda_{\max} = \frac{1}{n}\max_i |\langle \boldsymbol{d}_i\,, \boldsymbol{P}\rangle|$ and $\lambda_{\min} = 0.001\lambda_{\max}$[4].
2. Calculate the LASSO solutions for the given λ-sequence, starting from $\lambda_{\max}$, and save the descriptors $\boldsymbol{d}_i$ corresponding to the non-zero coefficients $\boldsymbol{c}_i$
3. Stop 2. at a chosen number N_{ℓ_1} of saved descriptors
4. Build a new matrix $\boldsymbol{D} \in \mathbb{R}^{n\times N_{\ell_1}+1}$ and apply the ℓ_0-method

Note, that in step 1, $\lambda_{\max}$ denotes the smallest λ, for which the LASSO solution is $\boldsymbol{c}^* = \boldsymbol{0}$ [27]. The method has shown to give low dimensional models with smaller RMSE than a pure ℓ_1-regularization. A drawback of the LASSO, is that sparse models with a high $\|\boldsymbol{c}\|_1$ are less preferred, and the *true* model of the ℓ_0-problem on the same feature space can be missed [1]. High coefficients occur for example, when descriptors are highly correlated, since otherwise (with not high coefficients) a linear combination of such almost parallel vectors would be a short vector, e.g. too short to describe a residual to $\boldsymbol{P}$. The motivation for the method is given by the following example.
Assume that $f(\boldsymbol{c}_{\text{true}})$ and $f(\boldsymbol{c}_a)$ are two k-dimensional descriptors with $\|\boldsymbol{P} - \boldsymbol{D}\boldsymbol{c}_{\text{true}}\|_2 < \|\boldsymbol{P} - \boldsymbol{D}\boldsymbol{c}_a\|_2$ and let $f(\boldsymbol{c}_{\text{true}})$ be the true model of the ℓ_0-problem, which is the best k-dimensional descriptor. Note that for a model $f(\boldsymbol{c}_r)$ with a bias, $\|\boldsymbol{P}-\boldsymbol{D}\boldsymbol{c}_r\|_2 = \|\boldsymbol{P}-\tilde{\boldsymbol{D}}\tilde{\boldsymbol{c}}_r\|_2$, where $\tilde{\boldsymbol{D}}$ is the standardized matrix and $\tilde{\boldsymbol{c}}$ the correspondingly transformed coefficients. If at a given λ the LASSO solutions[5] $\tilde{\boldsymbol{c}}_{\text{true},\lambda}$ and $\tilde{\boldsymbol{c}}_{a,\lambda}$ fulfill

$$\lambda(\|\tilde{\boldsymbol{c}}_{\text{true},\lambda}\|_1 - \|\tilde{\boldsymbol{c}}_{a,\lambda}\|_1) > \|\boldsymbol{P} - \tilde{\boldsymbol{D}}\tilde{\boldsymbol{c}}_{a,\lambda}\|_2^2 - \|\boldsymbol{P} - \tilde{\boldsymbol{D}}\tilde{\boldsymbol{c}}_{\text{true},\lambda}\|_2^2, \tag{3.21}$$

then $f(\tilde{\boldsymbol{c}}_{a,\lambda})$ will be preferred to $f(\tilde{\boldsymbol{c}}_{\text{true},\lambda})$. Thus $f(\boldsymbol{c}_{\text{true}})$ may be missed when applying LASSO.

---

[4] The number 120 is chosen empirically.

[5] Here a LASSO solution for a matrix with only the k columns of the corresponding model, $f(\boldsymbol{c}_{\text{true}})$ or $f(\boldsymbol{c}_a)$, is meant.

Now tuning down λ, will lead to less weight on the ℓ_1-score, such that on the one hand 3.21 does not hold anymore, but also higher dimensional descriptors are selected. Such higher dimensional descriptors may be a linear combination of the descriptors of $f(\tilde{\boldsymbol{c}}_{\text{true},\lambda})$ and a model $f(\tilde{\boldsymbol{c}}_{b,\lambda})$, where the latter is close to the residual $\boldsymbol{P} - f(\tilde{\boldsymbol{c}}_{\text{true},\lambda})$. By an ℓ_0-regularization, with a matrix $\boldsymbol{D}$, consisting of all descriptors in of $f(\tilde{\boldsymbol{c}}_{\text{true},\lambda})$ and $f(\tilde{\boldsymbol{c}}_{b,\lambda})$, the solution for the best k-dimensional descriptor will be $f(\boldsymbol{c}_{\text{true},\lambda})$. Hence the ℓ_1-ℓ_0 manage such cases[6].

3.6 Orthogonal matching pursuit

In this section the orthogonal matching pursuit (OMP) is presented, which gives the basis for the sure independent screening (SIS), presented in the next section. The OMP is a greedy algorithm, which finds at each iteration, the closest vector $\boldsymbol{d}_r$ to the current residual $\boldsymbol{R} = \boldsymbol{P} - f_{\text{current}}$ from the available set of descriptors $\{\boldsymbol{d}_i\}$,

$$\|\boldsymbol{R} - \boldsymbol{d}_r c_r\|_2^2 \leq \|\boldsymbol{R} - \boldsymbol{d}_i c_i\|_2^2 \tag{3.22}$$

for all $\boldsymbol{d_i} \in \{\boldsymbol{d}_i\}$ with corresponding least square solutions $\boldsymbol{c}_i$. It is characterized by its low computational complexity, which is a matrix multiplication $\boldsymbol{D}^T\boldsymbol{R}$ and find the index of the entry of the resulting vector with the highest absolute value, in each iteration. Thus the OMP can be applied to large feature spaces.
To find the $\boldsymbol{d}_r$, we assume that the descriptors $\boldsymbol{d}_i$ are standardized vectors and rewrite 3.22:

$$\|\boldsymbol{R} - \boldsymbol{d}_r c_r\|_2^2 + \|\boldsymbol{d}_r c_r\|_2^2 + \|\boldsymbol{d}_i c_i\|_2^2 \leq \|\boldsymbol{R} - \boldsymbol{d}_i c_i\|_2^2 + \|\boldsymbol{d}_r c_r\|_2^2 + \|\boldsymbol{d}_i c_i\|_2^2.$$

Since $\langle \boldsymbol{R} - \boldsymbol{d}_i c_i, \boldsymbol{d}_i c_i \rangle = 0$ and with the Pythagorean theorem:

$$\begin{aligned} &\Leftrightarrow \|\boldsymbol{R} - \boldsymbol{d}_r c_r + \boldsymbol{d}_r c_r\|_2^2 + \|\boldsymbol{d}_i c_i\|_2^2 \leq \|\boldsymbol{R} - \boldsymbol{d}_i c_i \ + \boldsymbol{d}_i c_i\|_2^2 + \|\boldsymbol{d}_r c_r\|_2^2 \\ &\Leftrightarrow \|\boldsymbol{d}_i c_i\|_2^2 \leq \|\boldsymbol{d}_r c_r\|_2^2 \\ &\Leftrightarrow |c_i| \leq |c_r|, \end{aligned}$$

since all $\boldsymbol{d}_i$ have same lengths $\|\boldsymbol{d}_i\|_2$. From Sec. 3.2 we know, that

$$|c_r| = \left| \frac{1}{\|\boldsymbol{d}_r\|_2^2} \langle \boldsymbol{R}, \boldsymbol{d}_r \rangle \right|. \tag{3.23}$$

---

[6] The presented scenario considers the case to find the true model. Nevertheless the method does not ensure, that the true model is found, but gives in general an improvement to results found directly by the LASSO for a desired k, e.g. in this scenario the true model can be replaced by another model, which has a lower MSE than the one, found by LASSO.

Hence, the closest vector to $\boldsymbol{R}$ is given by the $\boldsymbol{d}_i$ corresponding to the entry of the vector

$$\boldsymbol{D}^T\boldsymbol{R}. \tag{3.24}$$

with the largest absolute value. Hence, the OMP is applied in the following way. Note that $\boldsymbol{D}$ is standardized.

1. Initialize $\boldsymbol{R}_1 = \boldsymbol{P}$ and $X = \emptyset$ the set of saved descriptors. Chose a target dimension k for the linear model and let the iteration counter $j = 1$
2. Find the closest $\boldsymbol{d}_i$ to $\boldsymbol{R}_j$ and add it to X
3. Build the matrix $\boldsymbol{D}$ with all $\boldsymbol{d}_i \in X$. Calculate $\boldsymbol{c}^* = \arg\min_{\boldsymbol{c}\in\mathbb{R}^j} \|\boldsymbol{R}_j - \boldsymbol{D}\boldsymbol{c}\|_2$. Let $\boldsymbol{R}_{j+1} = \boldsymbol{R}_j - \boldsymbol{D}\boldsymbol{c}^*$
4. If $j = k$, stop. Otherwise set $j = j + 1$ and return to the 2. step

3.7 The SIS-ℓ_1-ℓ_0 method

In this section we present the scheme, used in this work. The method is called Sure-independent-screening-ℓ_1-ℓ_0 (SIS-ℓ_1-ℓ_0) [2] and is a subsequent application of the SIS [29] and the ℓ_1-ℓ_0 method. Here, the sure independence screening part generalizes the OMP in the sense that, in the 2. step, the $N_{\text{SIS}} \geq 1$ closest vectors to the current residual are saved. In the third step the best linear model is found by the ℓ_1-ℓ_0-method. In detail:

1. Initialize $\boldsymbol{R}_1 = \boldsymbol{P}$ and $X = \emptyset$ the set of saved descriptors. Chose a target dimension k for the linear model and let the iteration counter $j = 1$
2. Find the N_{SIS} closest $\boldsymbol{d}_i$ to $\boldsymbol{R}_j$ and add them to X
3. Build the matrix $\boldsymbol{D}$ with all $\boldsymbol{d}_i \in X$. Calculate the best j-dimensional descriptor $\boldsymbol{D}\boldsymbol{c}^*$, using the ℓ_1-ℓ_0-method. Let $\boldsymbol{R}_{j+1} = \boldsymbol{R}_j - \boldsymbol{D}\boldsymbol{c}^*$
4. If $j = k$, stop. Otherwise set $j = j + 1$ and return to the 2. step

Note, that in iteration $j = 1$, the best 1-dimensional descriptor is already given by the closest $\boldsymbol{d}_1$ to $\boldsymbol{R}_1$ in step 2. The method is controlled by the two parameters N_{SIS} and N_{ℓ_1}. After the SIS is applied (2. step) in an iteration j, the size of the current feature space is $j \cdot N_{\text{SIS}}$. The features selected by the SIS in an iteration are highly correlated with each other. As discussed in Sec. 3.5, the performance of the LASSO on feature spaces with high correlations is rather low. However, it is shown [2], that the combination of SIS and ℓ_1-ℓ_0 proves advantageous, compared to OMP. We will also apply the scheme with a ℓ_0-method in the 3. step instead of a ℓ_1-ℓ_0 for low dimensions k, as a benchmark.

If we are interested, in a multi-task problem, as presented in 3.4, in the 2. step a mean residual vector $\bar{\boldsymbol{R}}$ is constructed, where each entry with index i is the quadratic mean of the entries of the different property residuals with index i. In the multi-task ℓ_0-regularization, the combination of descriptors with the lowest quadratic mean of the RMSE of each property model is used in the 3. step in 3.3.

3.8 Cross-validation

The methods presented till now, are constructed to find the best linear fit to a property vector of n materials. Now, it is crucial, to investigate, its performance in predicting the same property for new materials. Especially when reducing the error of a fit, e.g. by increasing the complexity of the model, the risk of *overfitting* occurs. In our case the complexity of a model could be given by its dimension k. With higher k the models become more flexible, such that also *unimportant fluctuations* can be fitted, resulting in low predicting performance.
To judge the predicting quality, we apply a *10-fold-cross-validation* for a set K of dimensions of descriptor[7]:

1. Divide the set of n samples (Materials) into 10 subsets S_i of (almost) equal size, randomly distributed. Set the index $j = 1$.
2. Chose S_j as the *test* set, and build the union of the remaining 9 subsets, to be the *training* set.
3. Find for each $k \in K$ the best k-dimensional descriptor for the training set.
4. Calculate the found models with the descriptors corresponding to the materials of the test set, for each k. (prediction)
5. If not $j = 10$, continue with step 2. Otherwise calculate the RMSE between the values to be predicted and the predicted values for all n materials, for each k.

We will call the RMSE in step 5 the *prediction error*. We generally do several rounds of cross-validation and build the average over the prediction errors. The reason for considering all $k \in K$ at the same time, is that thereby their difference do not depend on the training/test set and thus they are more comparable. When applying a multi-task SIS-ℓ_1-ℓ_0, for each property vector (energy difference) the same materials are considered in a training set. For each property, a model is built on the training set, where the models distinguish themselves only by the size of the coefficients. The model of a chosen property vector is then evaluated on the compounds of the test set belonging to the same property vector, e.g. a model for a structure stability is only used to predict materials of the same structure stability.
Note that, with this type of cross-validation, we don't judge the prediction performance of a specific liner fit, but the prediction performance of the used technique with the given feature space. At each iteration a different model can be selected, describing the current training set best. Here, we validate the idea of using the best fit for a given training set and predicting the property of new materials.

---

[7] If for example we are interested in 1 and 2-dimensional descriptors, then $K = \{1, 2\}$

4 DFT calculations

4.1 Materials and structures

In this section, we describe how the reference data for the compressed-sensing investigation presented in Chap. 3 was calculated. The data set consists of 82 octet binary materials (see App. B for the list of materials), each optimized in 8 different crystal structures. The structures are selected from the Pettifor structure map for AB compounds [20] and listed in table 4.1. Not all 82 materials are known to crystallize in all 8 crystal structures, however, with LDA-DFT, at least one (possibly meta-stable) minimum is found for all materials and crystal structures. Details about the lattice vectors ($\boldsymbol{a}$, $\boldsymbol{b}$, $\boldsymbol{c}$), atomic coordinates and defined structural parameters (a, b, c, d, u and v) are found in App. B. The properties of interest, i.e., the total energy E_{tot} and the lattice parameters, are calculated in an (energy) minimum at each corresponding crystal symmetry. While the materials in cubic structures are characterized by one minimum, the materials in the structures with more than one degree of freedom can show multiple minima (see Sec. 4.3).

Table 4.1: Used crystal structures and their degrees of freedom

class	prototype	degrees of freedom	
		lattice	atomic coordinates
cubic	rocksalt (RS)	1	0
	zincblende (ZB)	1	0
	CsCl	1	0
	NaTi	1	0
hexagonal	NiAs	2	0
	CoSn	2	0
tetragonal	NbP	2	0
orthorhombic	CrB	3	2

4.2 Numerical settings for the electronic structure calculations

The total energies of the data are estimated to be converged below 10 meV per atom, the energy differences between structures below 5 meV and the lattice constants below 0.02Å[1]. A convergence test with respect to the k-points, integration grids, and basis set was done for 6 materials in the structures RS, ZB, CsCl, and NiAs. Here, from each octet group

---

[1] These estimates are based on tests performed on a subset of structures and materials (see App. C).

combination (i.e., I-VII, II-VI, etc.) one-two materials were chosen, e.g. MgS, NaCl, Si, GaSb, Ge, and AlSb. For the remaining structures, only the convergence with respect to the k-points was tested, with the materials MgS and Si. The convergence tests and details are represented in App. C. For each test, the convergence tolerances were set to 1 meV per atom.

Table 4.2: k-grid settings. The values for k-points and k-points density are given per reciprocal lattice vector $\boldsymbol{a}^*$,$\boldsymbol{b}^*$, and $\boldsymbol{c}^*$. In the case of CoSn, the variable γ is the double of the k-points density $\tilde{k}_{a^*}(k)$ of a^*, corresponding to 10 k-points, e.g. $\gamma = 2 \cdot \tilde{k}_{a^*}(10)$.

	k-points			k-points density [1/Å]			σ_{gaus}[eV]	reference mat.
	$\boldsymbol{a}^*$	$\boldsymbol{b}^*$	$\boldsymbol{c}^*$	$\boldsymbol{a}^*$	$\boldsymbol{b}^*$	$\boldsymbol{c}^*$		
RS		22			11.4		0.1	AlSb
ZB		14			7.2		0.01	Ge
CsCl		30			15.7		0.01	Ge
NaTi		20			11.2		0.1	Si
NiAs	25	25	25	12.2	12.2	25.4	0.1	GeSi
CoSn	10	10	γ	7.1	7.1	14.2	0.1	Si
NbP-α	20	20	20	10.6	10.6	14.1	0.1	Si
NbP-β	16	16	22	8.8	8.8	8.8	0.1	Si
CrB prim.	20	19	20	10.0	10.0	10.0	0.03	Si
CrB super	11	19	11	10.0	18.0	10.0	0.03	Si

All DFT calculations are performed with FHI-aims [9], using the local density approximation (LDA), based on the homogeneous electron gas quantum Monte Carlo calculations of Ceperley and Alder [21] for the correlation energy, as parametrized by Perdew and Wang 1992 [22]. No spin polarization is considered. The atomic ZORA relativistic correction [23] is applied. Tight settings for the numerical integration grids and 3rd tier basis set are used.[2] For each structure, a reference material that shows to need a relatively dense k-grid to be converged, is selected. For materials with a smaller volume of the reciprocal unit cell than the one of the reference material, $V^* < V^*_{\text{ref}}$, the reference converged k-grid is used, for $V^* > V^*_{\text{ref}}$ the corresponding reference k-points density per lattice vector. The used k-grids and k-grid densities are listed in table 4.2.

---

[2] Exception are a) some materials with hard converging self-consistency cycles, for which A or B of the AB compounds is calculated in 2nd tier and b) the CrB structure, for which 2nd tier is used for both A and B, because, due to the large number of degrees of freedom, the equilibria are obtained with a laborious procedure. In general, after a relaxation with tier 2 a further relaxation with tier 3 would not add much expensive calculations. However, the underlying technique requires an alternating relaxation, which could lead to more not converged calculations.

4.3 Techniques to find the equilibria

For all structures but CrB we use a fit to the Birch-Murnaghan (BM) equation of states, given by

$$E(V) = E_0 + \frac{B_0 V}{B_0'}\left[\frac{(V_0/V)^{B_0'}}{B_0'-1}+1\right] - \frac{B_0 V}{B_0'-1}, \tag{4.1}$$

where V_0 and E_0 are the equilibrium volume and energy, B_0 the bulk modulus and B_0' its derivative with respect to pressure. 5-8 volume *points* are used for the fit, with a linear sequence of lattice constants a, such that the highest/lowest value is $\tilde{a} \pm \frac{\gamma}{100}\tilde{a}$, where $\tilde{a}$ is a starting value close to the equilibrium lattice constant a_0. We call such a fit a *(5-8)-point BM-fit with a γ%-range*. Also for the hexagonal and tetragonal structures the a-parameter is used to build the sequence. The choice of γ is a compromise between a small range for accuracy (App. C) and a high range for including the equilibrium a_0.

The equilibrium properties of the cubic systems are obtained by a 5-point BM-fit with a 4%-range. The reason for applying the BM-fit-technique also for the non-cubic systems, is to ensure in an easy way, that the space group holds, i.e. that the lattice vectors $\boldsymbol{a}$ and $\boldsymbol{b}$ have same length in the case of NiAs. For these systems, the lattice parameter a is sampled. For each a the second parameter c (d in the case of NbP) is relaxed, using the geometry relaxation function in FHI-aims with the BFGS-algorithm and a tolerance value of below 10^{-4}eV/Å for the forces. For each relaxed point a volume and an energy are obtained to be used in a (5-8)-point BM-fit with a 4%-range [3]. To obtain the equilibrium a_0 and c_0 (d_0) from the equilibrium volume V_0, a second degree polynomial fit $c_{pol}(a)$ is used for the (a,c)-pairs (Fig. 4.1). In the case of NiAs for example, a_0 is calculated by solving the cell volume equation $V_0 = a^2 \cdot c \cdot \cos(30°) = a^2 \cdot c_{pol}(a) \cdot \cos(30°)$.

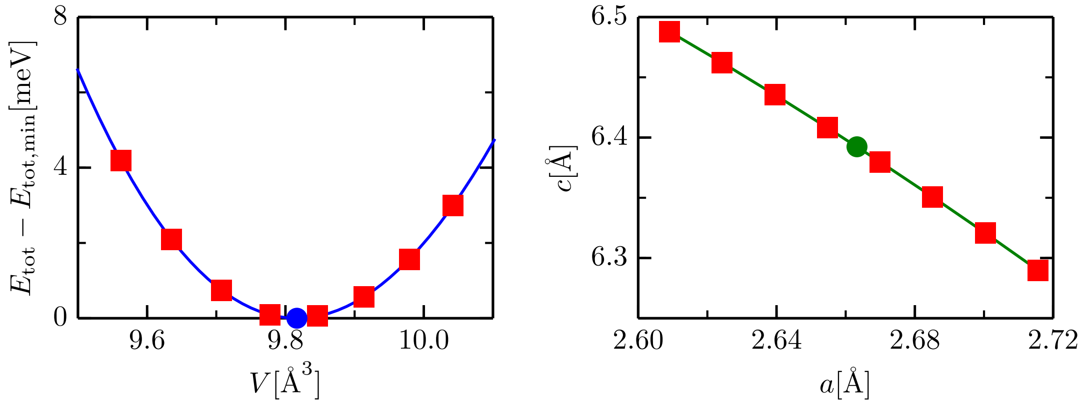

Figure 4.1: Fits to determine the equilibrium properties for CuF in the NiAs structure. The red squares represent the data to be fitted, the circles stand for the determined equilibrium. Left: 8-point BM-fit with a 4%-range. Right: second degree polynomial fit $c_{pol}(a)$.

The main effort in calculating the equilibrium properties is caused by the search for $\tilde{a}$, $\tilde{c}$

---

[3] For some materials a 4%-range along a correspond to a 6%-12% -range of c. For these cases a 1.5%-2% -range of a was set.

or $\tilde{d}$ with fixed crystal symmetry, described in the following. To obtain these equilibrium regions always the default basis set is used.

4.3.1 Cubic systems

In the case of CsCl and NaTi, $\tilde{a}$ is obtained by sampling the Energy surface with 50 points along $2.3\text{Å} < a < 7.8\text{Å}$ (CsCl) and 30 points along $4.5\text{Å} < a < 16.0\text{Å}$ (NaTi) for each material, using light grids and 4-8 k-points per lattice vector. For RS and ZB the a_0-values from the supplementary information of [10] are used.

4.3.2 NiAs

For the NiAs structure, the potential energy surface of ten materials, at least one for each octet combination group (I-VII, II-VI, etc.), is sampled, using a 50×50 grid, with 50 points along $1.8\text{Å} < a < 9.0\text{Å}$ and 50 along $1.8\text{Å} < c < 9.5\text{Å}$, with tight settings, $20 \times 20 \times 20$ k-points for III-V and IV-IV materials and $12 \times 12 \times 12$ k-points for the other materials[4]. For the considered 4th group materials Si and Ge, two minima were found, for the remaining materials one minimum was observed. For the higher-energy minimum of Si and Ge, the ratio c/a is 3.4 and 3.1, for the lower-energy minimum, 1.6 and 1.7. For the remaining considered materials, the ratio is $1.4 < c/a < 1.8$. The material NiAs shows a ratio $c/a = 1.4$, consistently the literature [17, 19]. To determine $\tilde{a}$ and $\tilde{c}$ for all materials, a unit cell relaxation with fixed angles between the lattice vectors, implemented in FHI-aims, is done with the NiAs literature values $a = 3.618\text{Å}$ and $c = 5.034\text{Å}$ ($c/a = 1.4$) as a start geometry. The BM-technique is applied afterwards, since the lenghts of the relaxed $\boldsymbol{a}$ and $\boldsymbol{b}$ can differ up to 0.01Å. $\tilde{a} = \frac{\|\boldsymbol{a}\|+\|\boldsymbol{b}\|}{2}$ and the relaxed c as $\tilde{c}$ is used.

4.3.3 CoSn

The CoSn structure depends on the order of the atom types in the unit cell, AB or BA, i.e., the two sites are not equivalent. Please note, that in this work A labels the element with the smaller electronegativity.

For the case BA, the potential-energy surface of all 82 materials is sampled, using a 45×45 grid along $2.3\text{Å} < a, c < 11.0\text{Å}$. Light settings and $8 \times 8 \times 14$ k-points are used. Except for the materials AlSb, GaSb, InSb[5] CC, BN, and BP, for all materials one minimum is found. On avarage, $c/a = 0.59$. For the exceptions two minima are found. For CC, BN,

---

[4] III-V and IV-IV materials show to have a rather small HOMO-LUMO gap and to need a relatively dense k-grid to be sufficiently converged.

[5] but not BSb

and BP one in the region $c/a = 0.52$ and one in a region $c/a > 1$. For all three cases, the minimum in the region $c/a = 0.52$ is lower in energy, thus only this minimum is considered. For AlSb, GaSb InSb both minima are in a region $0.52 < c/a < 0.8$. The energy difference between the two minima shows rather small values, 25 meV for AlSb, 4 meV for InSb and 50 meV for GaSb. For AlSb and and InSb, the considered region of the surface is additional sampled with a $25 \times 25 \times 25$ k-grid and no significant qualitative change is obtained. From this point, only the lower minima are considered.

For the AB case, in the first step the surface of the materials AlSb, CC, MgS, NaCl and is SiSi is sampled. The found minima are in a region $c/a = 0.67$, in values close to the one of the BA case. For the remaining materials, the surfaces are sampled along smaller ranges. Using a_{BA} and c_{BA} from the BA minimum, the considered ranges are $a_{\mathrm{BA}} - 3\text{Å} < a < a_{\mathrm{BA}} + 3\text{Å}$ and $c_{\mathrm{BA}} - 1.9\text{Å} < c < c_{\mathrm{BA}} + 2.5\text{Å}$.

For both, AB and BA, all materials are calculated in the found minima with converged settings. For the machine-learning part of this work, to each material the lowest minimum of the both cases is assigned.

4.3.4 NbP

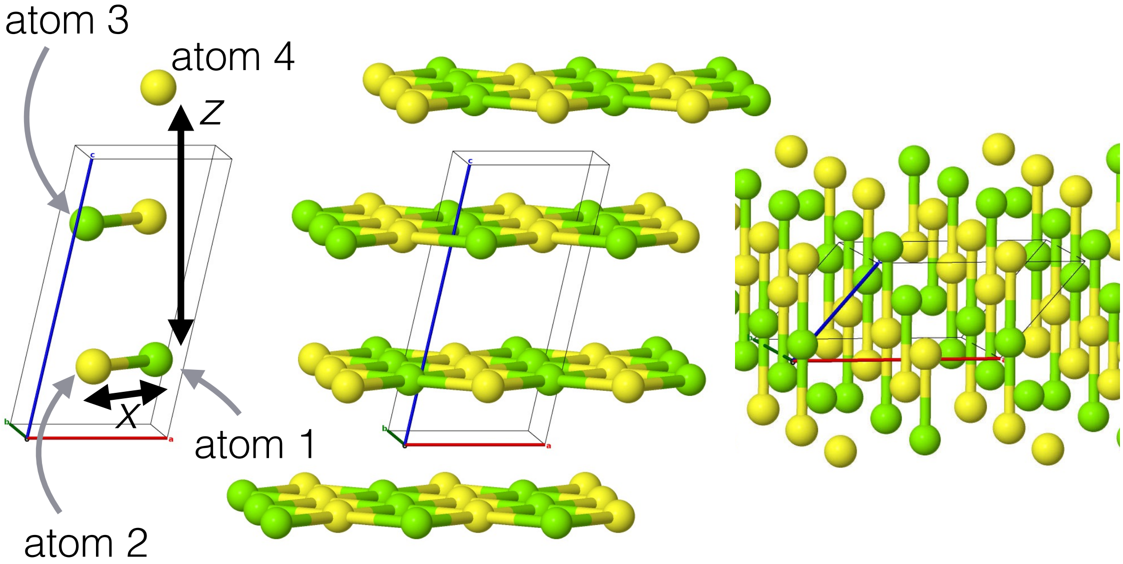

Figure 4.2: Geometry of MgS in the NbP structure. Left: Defined atoms and distances. Center: Geometry in the α-minimum. x is shorter than z. Right: Geometry in the β-minimum. z is shorter than x.

For the NbP structure, the potential-energy surface of all 82 materials is sampled. The observed ranges are $2\text{Å} < a < 10.4\text{Å}$ and $1.7\text{Å} < a < 16.2\text{Å}$. Light settings and $8 \times 8 \times 12$ k-points are used. Each material shows to have two minima, GaP, GaAs, GeSi, InAs, InSb and Si even three. We would like to assign two minima to each material, instead of one. We will characterize the minima using the criteria

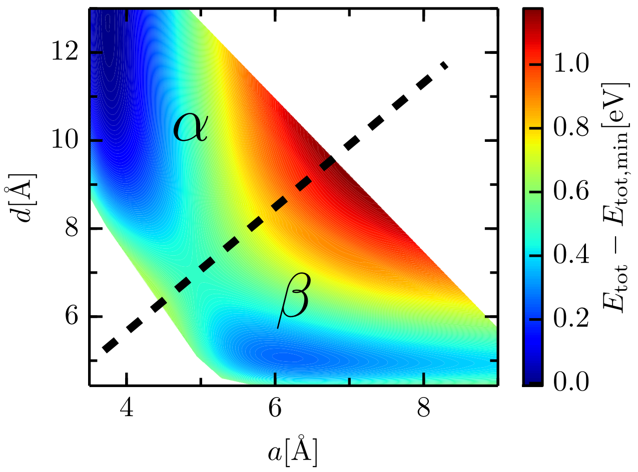

Figure 4.3: Surface contour plot of NaCl in the NbP structure. The contour plot is done for 955 points. Light settings, default basis set and $8 \times 8 \times 12$ k-points are used.

1) ratio $r = x/z$ of the atomic distances $x = \sqrt{\frac{1}{2}}a$ and $z = \frac{d}{2}$ (as drawn in figure 4.2, left)

2) the next neighbour to atom 1.

For all materials, one minimum is found in the region with $r > 1$, which we call β, and one minimum is found with $r < 1$, called α (Fig. 4.3). The ratios of the α-minima are even $r_\alpha < 0.62$ for all materials, except for Sn, with $r_{\alpha,\mathrm{Sn}} = 0.85$, and except for the *second* α-minimum of the materials GaP, GaAs, GeSi, InAs, InSb and Si, having $0.83 < r_\alpha < 0.93$. The nearest neighbor of atom 1 is atom 2 for all materials in the α-minimum, except for Sn and the materials in the second α-minimum. For these exceptions atom 3 is the nearest neighbor. In the case of the β-minimum, for 70 materials atom 4 is the nearest neighbor and for 12 materials (which are found to be III-V and IV-IV materials), atom 3 is the nearest neighbor. From this point, only two minima per material are taken into consideration: the beta minimum and the alpha minimum, with atom 2 as the nearest neighbor (except Sn, with atom 3).

4.3.5 CrB

The CrB structure has 5 degrees of freedom, the lattice parameters a, b, and c, and two atomic cooridinate parameters u and v. The values for the CrB material are listed and compared to the literature values in table 4.3.

To obtain the equilibrium, alternately the unit cell and the atoms are relaxed, until the forces are below $5 \cdot 10^{-3}$[eV/Å]. For the cell relaxation the orthorhombic super cell is used, with fixed angles in FHI-aims. For the atoms relaxation the primitve unite cell is used, and the forces are projected on the vector $-\boldsymbol{a} + \boldsymbol{b}$, in order that only movements along $-\boldsymbol{a} + \boldsymbol{b}$

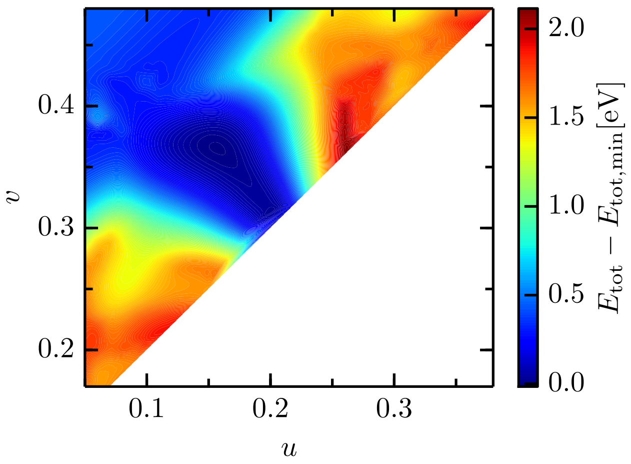

Figure 4.4: u-v-surface contour plot for MgS in the CrB structure. For 565 pairs (u,v), the unit cell was relaxed with with fixed u and v, with the relaxation start values $a = 3.60$,$b = 9.69$,and $c = 3.60$ and fixed angles. Tight settings, default basis set and $8 \times 8 \times 12$ k-points are used.

are allowed. Please note that the parameters a, b and c are the lengths of lattice vectors of the orthorhombic super cell, while in the case of the primitive cell $\|\boldsymbol{a}\| = \|\boldsymbol{b}\| = \frac{1}{2}\sqrt{a^2 + b^2}$. A test on the materials MgS, Nacl and Si with the literature values of 4.4 shows, that depending on what is relaxed first, lattice or atoms, two different minima can be found, listed in table 4.4. A u-v-surface plot for MgS is shown in figure 4.4. The first minimum of table 4.4 (cell first) is not found in the surface, because the (u,v)-pair $(0.09, 0.39)$ is a minimum for a cell with a ratio b/c close to 1. The parameters of the relaxed cell at $(0.09, 0.39)$ on the represented surface are $a = 3.36$, $b = 13.54$, and $c = 3.62$.

In order to relax all 82 materials in the CrB structure, initial relaxation parameters in the area of the average of the lower minima in table 4.4 are used, $a = c$, $b/a = 3.3$, $u = 0.16$ and $v = 0.38$. The initial cell volume $V_{\mathrm{CrB,mat}}$ for each material is determined by scaling with respect to MgS,

$$V_{\mathrm{CrB,mat}} = \frac{V_{\mathrm{RS,mat}} + V_{\mathrm{ZB,mat}}}{V_{\mathrm{RS,MgS}} + V_{\mathrm{ZB,MgS}}} \cdot V_{\mathrm{CrB,MgS}}. \tag{4.2}$$

The technique to obtain the minimum now is: While alternately relaxing cell and atoms,

Table 4.3: Structural parameters of the material CrB. Calculated values or compared to experimental literature values [18, 19] For the calculation, tight settings, default basis set and $20 \times 10 \times 20$ k-points are used.

	calculated	literature
a	2.87	2.98
b	7.72	7.87
c	2.87	2.93
u	0.146	0.146
v	0.436	0.440

Table 4.4: Structural parameters of the material CrB. For the calculation, tight settings, default basis set and 20 × 10 × 20 k-points are used.

	relaxation first for	a	b	c	u	v	E_{tot} [eV]
MgS	cell	3.74	7.57	6.38	0.09	0.39	-8141.094
	atoms	3.52	12.16	3.56	0.17	0.37	-8141.392
NaCl	cell	3.65	11.42	3.99	0.13	0.37	-8475.292
	atoms	3.65	11.42	3.99	0.13	0.37	-8475.292
Si	cell	3.23	9.21	3.98	0.11	0.39	-7873.766
	atoms	3.42	10.19	3.44	0.16	0.41	-7873.800

each *round* of cell/atoms relaxation, the cell or atoms are not fully relaxed (below the forces tolerance) but only up to several BFGS-steps. Starting with 1 step in the first round, the BFGS-steps are increased each round 1-2 steps.

For each material the relaxation is started with once relaxing the cell first and once relaxing the atoms first. In this case, always one minimum is found, except for AgBr, where two different minima are obtained and the lowest-energy minimum is considered.

5 Machine learning

5.1 Primary features

Although the two-dimensional *descriptors* (parameters describing the materials) proposed by Mooser and Pearson [11] and by Phillips and Van Vechten [13, 14, 15] were able to satisfactorily classify the octet binaries, they do not fulfill one important criteria of this work. The determination of those material parameters implies already the knowledge of which is the most stable material. In practice, in a computational setting, one would have to first optimize the crystal structures and, for the energetically most stable, calculate the descriptor for predicting the stability itself. It should be recognized that such descriptors, computationally as expensive as directly calculating the property of interest, can still help to understand important underlying mechanisms. However, similar descriptors cannot be predictive, i.e., help discovering *new* materials, because the material has to be known in order to calculate its descriptor. The demands in our work are set higher: The use of machine learning shall provide the opportunity to discover new promising materials much faster. Thus, the descriptors are restricted to be determined with (much) less expensive calculations than for the property to be predicted.

In this work, we call *primary features* a set of basic candidate parameters describing the materials, that are expected to determine the property of interest. We call *derive features*, or simply *features* a possibly large set of, in general non-linear, functions (algebraic combinations) of the primary features.

The descriptor (r_σ,r_π) of St. John and Bloch [16], already mentioned in the introduction, based on orbitally dependent radii r_σ and r_π gives a good starting point. The two dimesion of the descriptor are defined as:

$$\begin{aligned} r_\pi &= |r_p(\mathrm{A}) - r_s(\mathrm{A})| + |r_p(\mathrm{B}) - r_s(\mathrm{B})| \\ r_\sigma &= |[r_p(\mathrm{A}) + r_s(\mathrm{A})] - [r_p(\mathrm{B}) + r_s(\mathrm{B})]|. \end{aligned}$$

In their work St. John and Bloch analytically solved the radial part of a Schrödinger equation describing the one electron valence states. Their solution yields the eigenvalues

$$E(n,l) = -\frac{Z^2}{2(n + \hat{l}(l) - l)^2}. \tag{5.1}$$

With the parameter $\hat{l}$ depending on the angular momentum quantum number l, which was determined by fitting Eq. (5.1) to experimental results. They then defined the radii r_l as the radial maximum of the lowest valence eigenfunction

$$r_l = \frac{\hat{l}(\hat{l}+1)}{Z}. \tag{5.2}$$

In analogy to St. John and Bloch's work, Ghiringhelli *et al.* [10] included the atomic-orbital radii r_s, r_p, r_d from DFT-calculations, as the radii at which the radial part of probability density has its maximum. As done in Ghiringhelli *et al.*'s work, we include these radii, the highest occupied and lowest unoccupied KS level (HOMO and LUMO), and the ionization potential (IP) and the electron affinity (EA) of the atoms. Although the IP and EA contribute with similar information as the HOMO and LUMO, complicated algebraic combinations are expected to yield to different derived features. With these primary features, Ghiringhelli *et al.* described the energy differences of the considered 82 octet binaries between RS and ZB, with 65% lower error than with (r_σ,r_π)[1]. Furthermore, we include the atomic number N and the number of valence electrons N_{val}. Besides atomic information, for the AB compounds also the dimer distances $d_{\text{dim}}^{\text{AB}}$, $d_{\text{dim}}^{\text{AA}}$ and $d_{\text{dim}}^{\text{BB}}$ are considered. A further meaningful parameter, the Madelung energy E_{Mad} is considered. As discussed in Pettifor's book [20], the Madelung energy provides an intriguingly easy way to assess the relative stability of ionic crystals. However it is important to note that the Madelung energy depends on the geometry of the given material. Since the geometries are obtained in our case by the same calculations as the energies, a *representative* Madelung enregy is included, which is determined in a first step by primary features[2]. Note that, we rather include the *reduced* E_{Mad} (see Eq. 2.40) with neglected charges, in this work. Without neglecting the charge given by the number of valence electrons, for IV-IV binaries the Madelung energy ought to be 0. More *constructively*, it makes sense to consider only monovalent ions (charge +/-1) so that the reduced Madelung energy is just an encoding, a descriptor, of the geometrical structure, while electronic information is in the EA, IP, etc.. In the considered feature spaces also features with the prodcts as $\text{EN}^2 \cdot E_{\text{Mad}}$ are constructed, giving a reasonable scale for a *realistic* non-reduced Madelung energy, where $\text{EN} = \frac{1}{2}(\text{IP} + \text{EA})$ is the electronegativity.

5.2 Formulation of the problem

Given 82 materials, with their calculated DFT energies in 8 different crystal structures (see Chap. 4), the formulation of the problem and combining it with the statistical methods is not trivial; namely, the challenge is to obtain an accurate and sparse description of complicated materials-science properties (i.e., in this case the crystal structure energy differences). It specifies the target, the mathematical description and the demands on the

---

[1] Note, that here not the rate of classification is addressed but the error on predicted energy difference values for RS vs. ZB

[2] The assumption is, that geometries are easier to describe/predict then energy differences. Indeed, if the ratio RMSE/σ is as comparison measurement, the models for the geometry dependent quantities are better fitted, as presented in Sec. 5.6.2.

descriptors to describe the desired properties. One example could be focusing on predicting the cohesive energies of 82 materials, where each material is in its ground state. Another example could be predicting the energies of the 82 materials in one structure with the same geometrical parameters, e.g. all in RS with $a = 5$ Å. Finding the equilibrium energy could then be the next step with a formulation of a new problem. Depending on the target, the right statistical method must be used and the considered data has to be integrated correctly.

We are interested in describing the relative stabilities of the 82 compounds, e.g. their energy differences between two structures with a given set of features. An example for a derived feature could be $\frac{\mathrm{EA(A)}^2}{r_s(\mathrm{B})}$, where EA(A) is the electron affinity of atom A and r_s(B) the valence-s orbital radius of atom B. We consider only energy differences, relative to ZB. This gives 7 energy differences $\mathit{\Delta} E_{\text{X-ZB}}$, where $X \in \{\text{RS, CsCl, NaTi, NiAs, CoSn, NbP}\}$. For a considered structure X, we would like to find a linear combination of only a few features out of the feature space, which describe $\mathit{\Delta} E_{\text{X-ZB}}$ of the 82 materials accurately. The property vector $\boldsymbol{P}_X \in \mathbb{R}^{82}$ is constructed, out of the energy differences $\mathit{\Delta} E_{\text{X-ZB}}$ of the 82 materials. Given a feature space of size m, for each feature a descriptor column $\boldsymbol{d}_i \in \mathbb{R}^{82}$ is built, in which each entry is the feature evaluated for a compound. The order of the compounds in $\boldsymbol{d}_i$ is the same as the one in $\boldsymbol{P}_X$. Finally the m descriptors $\boldsymbol{d}_i$ are formed to a descriptor matrix $\boldsymbol{D} \in \mathbb{R}^{82 \times m}$. A linear model f of our interest can be written in the form

$$f(\boldsymbol{c}) = \boldsymbol{D}\boldsymbol{c}, \tag{5.3}$$

where the most entries of the coefficient vector $\boldsymbol{c} \in \mathbb{R}^m$ are 0. We say, that the model is a *k-dimensional descriptor*, if f is a linear combination of $k \in \mathbb{N}$ descriptors $\boldsymbol{d}_i$, e.g.

$$\boldsymbol{d}_{i_1} c_{i_1} + \boldsymbol{d}_{i_2} c_{i_2} + \ldots + \boldsymbol{d}_{i_k} c_{i_k}. \tag{5.4}$$

The task to find a model for a case $\mathit{\Delta} E_{\text{X-ZB}}$ is formulated:

1. Find a linear model $f_X(\boldsymbol{c}) = \boldsymbol{D}\boldsymbol{c}$, such that most of the entries of $\boldsymbol{c}$ are 0.
2. Find a linear model f_X, such that $\boldsymbol{P}_X \approx \boldsymbol{D}\boldsymbol{c}$.

The task is written in 3.3 (ℓ_0-regularization), to which solutions can only be found combinatorially. Hence, the problem can only be solved for small feature spaces and dimensions k in a reasonable time. In this work, the SIS-ℓ_1-ℓ_0 method (see Sec. 3.7) is applied, as an approximation to the ℓ_0-regularization, scanning feature spaces of above 10^{10} for models with $k \leq 7$.

A further step is done, by demanding different models f_X for different energy differences $\mathit{\Delta} E_{\text{X-ZB}}$, which consist all of the same descriptors $\boldsymbol{d}_i$. The different models f_X are just distinguished by their coefficients. The coefficients act as *weights* on the descriptors $\boldsymbol{d}_i$, depending on the structure. We call the set of such models a *multi-task-model* and the underlying mathematical problem a *multi-task problem.* The realization of solving a multi-task problem with SIS-ℓ_1-ℓ_0 method is demonstrated in Sec. 3.4.1 and Sec. 3.7.

5.3 Construction of the feature space

We will consider three different sets of primary features in this work:

$$\begin{aligned} F_{19} = \{&\mathrm{IP(A)},\ \mathrm{IP(B)},\ \mathrm{EA(A)},\ \mathrm{EA(B)},\ \mathrm{HOMO(A)},\ \mathrm{HOMO(B)},\ \mathrm{LUMO(A)},\ \mathrm{LUMO(B)},\\ &r_s(\mathrm{A}),\ r_s(\mathrm{B}),\ r_p(\mathrm{A}),\ r_s(\mathrm{B}),\ r_d(\mathrm{A}),\ r_d(\mathrm{B}),\ d_{\mathrm{dim}}^{\mathrm{AB}},\ N(\mathrm{A}),\ N(\mathrm{B}),\ N_{\mathrm{val}}(\mathrm{A}),\ N_{\mathrm{val}}(\mathrm{B})\} \end{aligned}$$

and unions

$$\begin{aligned} F_{21} &= F_{19} \bigcup \{d_{\mathrm{dim}}^{\mathrm{AB}},\ d_{\mathrm{dim}}^{\mathrm{AA}},\ d_{\mathrm{dim}}^{\mathrm{BB}}\} \\ F_{\mathrm{mad}} &= F_{19} \bigcup \{E_{\mathrm{Mad}}^{\mathrm{X}},\ E_{\mathrm{Mad}}^{\mathrm{ZB}}\}. \end{aligned}$$

The sets will be used in different cases. Note that $E_{\mathrm{Mad}}^{\mathrm{X}}$ labels the Madelung energy of a material in a structure X, when an energy differenc $\Delta E_{X-\mathrm{ZB}}$ is considered.
Given a set of primary features F, new features are built by applying the operations $\{x+y,\ x-y,\ x\cdot y,\ x\,/\,y,\ x^2,\ x^3,\ \exp(x)\}$ on $x, y \in F$. New descriptor columns $\boldsymbol{d}_i$ are then constructed, e.g. each entry of the column is filled with the new combination $x(\mathrm{A}) + y(\mathrm{B})$ with the entry corresponding to the compound AB. With this larger set of available descriptors $\boldsymbol{d}_i$, the SIS-ℓ_1-ℓ_0 method can be applied. The resulting models may then be linear models of non-linear functions of the given primary features. This procedure can be repeated on the just generated features space, e.g. $\frac{x(\mathrm{A})+y(\mathrm{B})}{\exp(z(A))}$, where also $z \in F$. To express a resulting feature space in dependence of the number of repetitions, we define the symbol

$$\mathcal{C}_i(F) \tag{5.5}$$

with the procedure repeated i times and $\mathcal{C}_0(F) = F$. We say, that a feature space $\mathcal{C}_{j+1}(F)$ contains more *complex* features then a space $\mathcal{C}_j(F)$[3]. While generating new features, we forbid sums and differences of features with different physical units, e.g. operations as $size + energy$ or $size + size^2$ are excluded. Furthermore, the resulting features are constrained to depend on both elements of a compound, A and B. Since the models of the SIS-ℓ_1-ℓ_0 are characterized by descriptors, where the descriptor from the first iteration gives the main contribution to the fit, this contribution will be given by both elements. Note that $|\mathcal{C}_1(F_{19})| \approx 400$, $|\mathcal{C}_2(F_{19})| \approx 3 \cdot 10^5$ and $|\mathcal{C}_3(F_{19})| \approx 10^{10}$.

5.4 Complexity of the feature space

In this section, the performance of the models, obtained by the SIS-ℓ_1-ℓ_0 method, in dependence on the complexity is testes. The test is done with the primary features F_{19} for the case RS-ZB, see Fig. 5.1. While for higher dimensions k of the descriptors, the RMSE shows a convergent behaviour from $\mathcal{C}_0$ till $\mathcal{C}_3$, for lower k, the highest improvement

---

[3] We include also all less complex features from the steps before. Thus not all, but most features of $\mathcal{C}_{j+1}(F)$ are more complex.

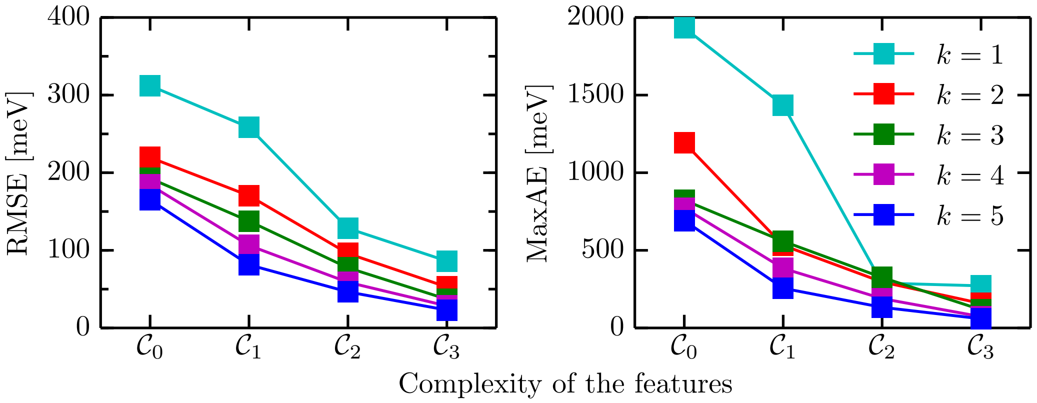

Figure 5.1: Dependence of the RMSE (left) and maximum absolute error (right) on the complexity of the feature space. The values are given by fits on the energy difference between RS and ZB for all 82 materials with the primary features F_{19}. The SIS-ℓ_1-ℓ_0 parameters are $N_{\text{SIS}} = 500$ and $N_{\ell_1} = 80$.

is observed from $\mathcal{C}_1$ to $\mathcal{C}_2$. The maximum absolute error (MaxAE) behaves similar. For $\mathcal{C}_0$ with $k \leq 4$ and $\mathcal{C}_1$ with $k \leq 2$, the MaxAE is given by diamond, which shows also the highest absolute value (2628 meV) of the energy differences (see Fig. 5.2). In the case $\mathcal{C}_3$ and $k = 1$ the model is sufficiently complex, to describe diamond with a error below 100 meV, for $\mathcal{C}_3$ and $k \geq 2$ even below 50 meV. For all following calculations, $\mathcal{C}_3$ is applied.

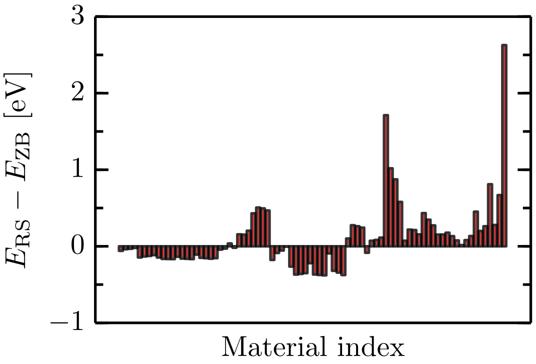

Figure 5.2: Energy difference between RS and ZB for the 82 materials. The standard deviation is 0.444 eV, the mean 0.106 eV. The maximum value 2.628 eV corresponds do diamond.

5.5 Setting the SIS-ℓ_1-ℓ_0 parameters

The SIS-ℓ_1-ℓ_0 method is controlled by the two parameters N_{SIS} and N_{ℓ_1}. In each iteration j, after the SIS is applied, the feature space has the reduced size of $j \cdot N_{\text{SIS}}$, following by a further reduction to N_{ℓ_1} by the LASSO. Finally the ℓ_0 method is applied to the feature space of size N_{ℓ_1}, and a j dimensional descriptor obtained is obtained (see Sec. 3.7).

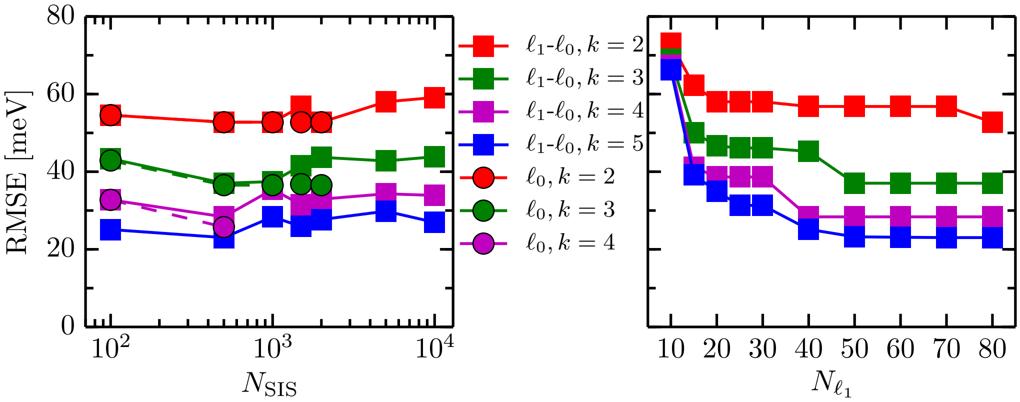

Figure 5.3: Dependence of the RMSE on the SIS-ℓ_1-ℓ_0 parameters N_{SIS} and N_{ℓ_1}. The values are given by fits on the energy difference between RS and ZB for all 82 materials. The feature space $\mathcal{C}_3(F_{19})$ is used. The data points given by the circles (left) are obtained by a SIS-ℓ_0 method, in which an ℓ_0 regularization is applied on the feature space obtained by SIS, in each iteration. When varying N_{SIS} (left), $N_{\ell_1} = 80$ is used. When varying N_{ℓ_1} (right), $N_{\text{SIS}} = 500$ is used.

The used SIS-ℓ_1-ℓ_0 parameters in this work are $N_{\text{SIS}} = 500$ and $N_{\ell_1} = 80$. It is observed, that for all considered dimensions k of descriptor, $N_{\text{SIS}} = 500$ gives the lowest RMSE (see Fig. 5.3). The increase of the RMSE for $N_{\text{SIS}} > 500$ is expected to be caused by the fact, that the SIS provides more correlated features, on which the LASSO shows rather low performances, as discussed in Sec. 3.7 and 3.5. The both obtained models $f_{N_{\text{SIS}}=500,k=4}$ and $f_{N_{\text{SIS}}=1000,k=4}$ are investigated in the following.

We will refer to the both cases with case $A = \{N_{\text{SIS}} = 1000, k = 4\}$ and case $B = \{N_{\text{SIS}} = 1000, k = 4\}$. The four descriptors of the model f_A are found in the LASSO step as descriptors of a LASSO model g_A, being a linear combination of 26 descriptors, which occurred at a $\lambda = 0.050$. The descriptors of f_A do not occur at any considered λ in the LASSO step of case B. The four descriptors of f_B, are contained in a 43 dimensional model g_B, which occurred at $\lambda = 0.014$[4]. Two matrices $\boldsymbol{D}_A \in \mathbb{R}^{82\times 26}$ and $\boldsymbol{D}_B \in \mathbb{R}^{82\times 43}$ are built and compared, using the LASSO. It is observed that for all $\lambda < 0.15$, $\boldsymbol{D}_B$ gives a lower LASSO score. Hence, g_B is preferred to g_A.

By increasing N_{SIS}, more possible models are offered, to be *discovered* by the ℓ_1-ℓ_0 -method, but, if a good sparse model can be obtained by a low N_{SIS}, the probability to find it can be decreased with a higher N_{SIS}.

Furthermore, it is observed that only in the case $\{N_{\text{SIS}} = 100, k = 2\}$, the solution of ℓ_1-ℓ_0 and ℓ_0 coincide[5]. In general the lower the k is, the closer is the RMSE of the models found by ℓ_1-ℓ_0 to the RMSE of the models found by ℓ_0.

Varying N_{ℓ_1}, shows that the RMSE is more sensitive for higher k values(see Fig. 5.3, on

---

[4] Please note, that we are not interested in the absolute values, since they will depend on the used scaling in front of the ℓ_2-norm of the LASSO. In all cases, the same λ-sequence is used, since $\lambda_{\max}$ is determined by the closest descriptor $\boldsymbol{d}_i$ to $\boldsymbol{P}$. Thus the λ-sequence is given by the total feature space.

[5] This is also true for all cases of $k = 1$.

the right). From $N_{\ell_1} = 50$ and higher, no further improvements are obtained, except in the case $k = 2$. For all following calculations a $N_{\ell_1} = 80$ is chosen, to ensure low errors also for higher dimensions of k with acceptable computational cost.

5.6 Results

5.6.1 Fitting performance for F_{19}

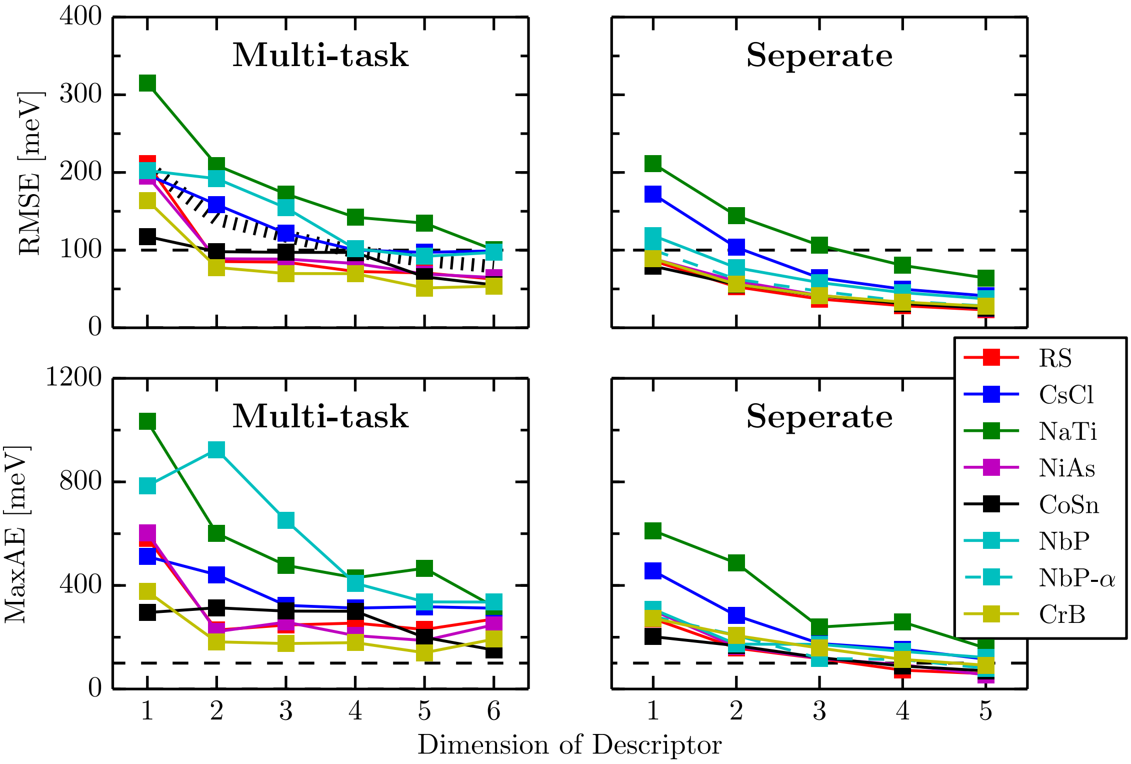

Figure 5.4: RMSE and MaxAE for multi-task and separate models. All considered structure stabilities, are build relative to ZB. The dotted line (upper left) denotes the quadratic mean over the RMSE lines of the seven stabilities.

A multi-task SIS-ℓ_1-ℓ_0 was applied on seven structure energy differences, where all differences are built to ZB. The found 6 dimensional descriptor, consisting of the same descriptor columns $\boldsymbol{d}_i$ for all energy differences with different sizes of the coefficients (weights on the descriptors), achieve RMSEs below 100 meV (see Fig. 5.4, upper left). The highest errors are achieved with the structures NaTi, NbP and CsCl. The energy difference data of NaTi and CsCl exhibits relatively high standard deviations σ (see Tab. 5.1). For the case $k = 6$, the ratio RMSE/σ shows comparable values between 10% and 15%, for all structures, except NbP [6]. For NbP, the ratio is 26%.

The multi-task results show higher values, than the models built separately for each relative stability. The difference becomes lower for higher dimensions k. For $k = 1$, the

---

[6] The standard deviation is the same as the RMSE of a fit $\boldsymbol{\mu}$, full of entries with mean μ of $\boldsymbol{P}$.

(quadratic) averaged RMSE of the multi-task models is 80 meV higher than the one of the separate models, while For $k = 5$ the difference is 50 meV.
The constraint by the multi-task method becomes more apparent, considering the MaxAE. For a chosen relative stability, we consider by which materials the MaxAE is given for $1 \leq k \leq 6$. For example in the case of the multi-task model for CoSn, for $k = 5$ the MaxAE is given by InP, for all remaining k-values it is given by LiI. So for this case the MaxAE is given by only 2 different materials along the different k-values. For the separately built models, the MaxAE is given by 3-5 different materials per structure stability, among the 5 different dimensions k. In contrast, in the multi task case, only 1-3 different materials are observed over the six k-values for a given structure stability, e.g. for RS-ZB for all six k values the MaxAE is given by AlN.
The found multi-task descriptors are shown in App. A.
A further separate model is built, using all 82 NbP-α minima as the data input, which shows a lower RMSE than the model obtained by using the global minima. Considering the performance relative to the standard deviations $\sigma_{\text{NbP}} = 376$ meV and $\sigma_{\text{NbP-}\alpha} = 470$ meV, the qualitative difference is even higher. This shows, that the demands on the descriptors can be lower, when one goes beyond our formulation of the problem (see Sec. 5.2), in which the materials are considered in the global minimum of a given structure as.

Table 5.1: Standard deviations of relative energies ΔE_{X-ZB} built to ZB, of Madelung energy E_{Mad} and Lattice constants. For CrB, only ΔE_{X-ZB} is considered in this work.

	$\sigma_{\Delta E_{X-ZB}}$ [meV]	$\sigma_{E_{\text{Mad}}}$ [meV]	σ_{Lat}[Å]
ZB	-	901	1.01
RS	444	818	0.85
CsCl	800	680	0.47
NaTi	873	536	0.89
NiAs	463	798	$\sigma_a = 0.59$, $\sigma_c = 1.08$
CoSn	540	801	$\sigma_a = 0.90$, $\sigma_c = 0.78$
NbP	376	924	$\sigma_a = 0.81$, $\sigma_d = 2.59$
NbP-α	470	877	$\sigma_a = 0.65$, $\sigma_d = 1.47$
CrB	448	-	-

5.6.2 Fitting performance for F_{mad}

In this section the inclusion of the Madelung energy E_{Mad}, as a primary feature, is considered. The target is to determine E_{Mad} from the primary features $\mathcal{C}_3(F_{21})$, in the first step. In the second step, the fitted E_{Mad} is included in the set of primary features, so that models are built from $\mathcal{C}_3(F_{\text{Mad}})$ to describe the relative structure stabilities. For the first step, two options are investigated. One is, building models, to fit E_{Mad} directly. The other is, to determine E_{Mad} by fitted lattice constants. To become acquainted with this technique the data of CrB-ZB is excluded, since the geometry of the CrB structure is

characterized by five degrees of freedom.
At the beginning of this section the inclusion of E_{Mad}, obtained from the geometries from the DFT calculations, is investigated. Then the two options, to determine E_{Mad} from $\mathcal{C}_3(F_{21})$, are analysed. Afterwards the influence of the errors from the first step on the final models is studied.

In Fig. (5.5), the results of the multi-task models, built from the feature space $\mathcal{C}_3(F_{\mathrm{Mad}})$ with E_{Mad}, obtained from the DFT geometries, are compared to models from $\mathcal{C}_3(F_{19})$. For all seven k values, the found descriptors consist of E_{Mad}. Although the improvements in RMSE are not significant (< 11 meV), they are increasing with increasing k. A decrease is obtained in the case $k = 2$. Here, one descriptor of the 2 dimensional model from $\mathcal{C}_3(F_{19})$, is not included in the feature space, which was reduced from $\mathcal{C}_3(F_{\mathrm{Mad}})$ by SIS. For the MaxAE, an alternating behaviour is observed.

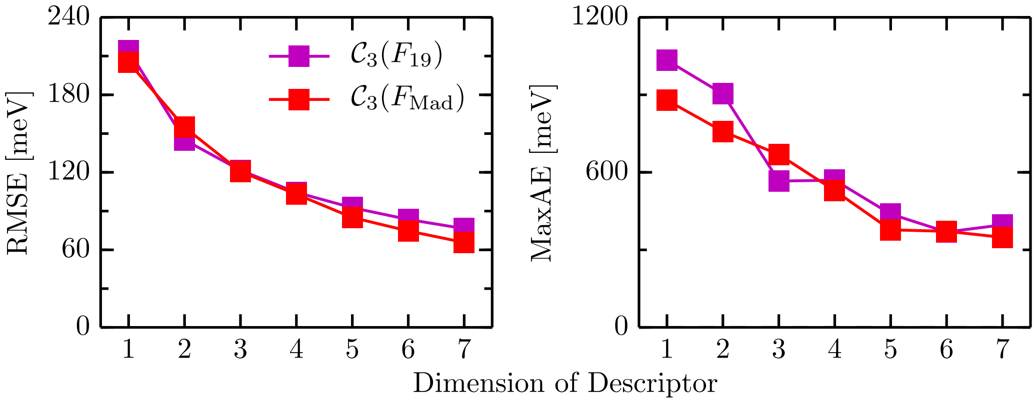

Figure 5.5: Performance of multi-task models from the feature spaces $\mathcal{C}_3(F_{19})$ and $\mathcal{C}_3(F_{\mathrm{Mad}})$. All considered structure stabilities, are build relative to ZB. On the left, the quadratic mean of the RMSE over all considered structure stabilities is shown. On the right the over all maximum error (per dimension) is shown.

The models for the lattice constants, are built separately for each structure. For structures, depending on two lattice constants, the models are obtained from a multi-task problem with both properties. The results are represented in Fig. 5.6. The lowest RMSE is obtained by cubic structures, the highest by NbP and NbP-α.
In both cases NbP and NbP-α, the d parameter exhibits a higher RMSE than a. We note that, for NbP-α, 8.27 Å $< d <$ 15.46 Å with a mean of 12.21 Å, and for NbP, 2.55 Å $< d <$ 15.46 Å with a mean of 11.69 Å. In the case of NbP (global minimum), 7 materials are in the β minimum, the rest is in the α minimum. Thus the obtained models suffer from the high variances between the two geometries. Improvements could be obtained, by building separate models for each parameter or considering atomic distances, instead of lattice constants. Both options are not considered in the frame of this work.
Exluding NbP and NbP-α, the RMSE/σ-values of the models for the geometries are lower than the ones for the energy differences. Now, values of or below 11% are achieved, for the

cubic structures even below 5%, e.g. for ZB RMSE/$\sigma_{k=5} = 0.02$.
The found multi-task descriptors are shown in App. A.

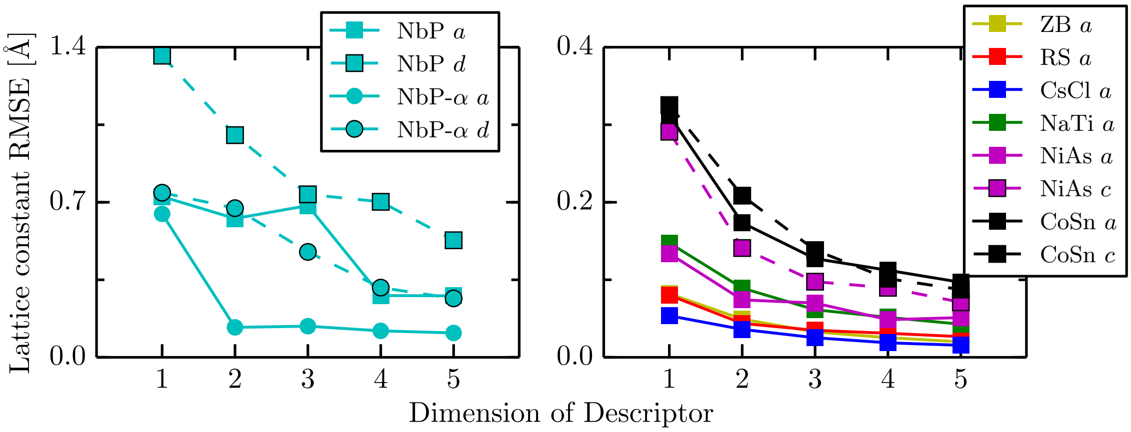

Figure 5.6: RMSE for models built to describe the lattice constants. NbP is shown separately in the left, with a larger y-range.

Next, E_{Mad} is calculated from the models built on the lattice parameters, and compared with the E_{Mad}-values, calculated from the DFT geometries (see Fig. 5.7, on the left and in the center). The obtained performances reflect the ones from Fig. 5.6. For the NbP case with $k = 2$, the MaxAE is 10.097 eV, given by diamond. For diamond, $a = 6.60$Å and $c = 2.55$Å ($c/a = 2.59$), while the fits to the lattice constants give $f_a = 5.86$Å and $f_c = 1.12$Å ($f_c/f_a = 5.23$).
Furthermore models were build to fit E_{Mad} directly (see Fig. 5.7, right). For $k = 5$, the RMSE/σ-values are all below 5%. For the cubic systems, the results are comparable with the results of the models for the lattice constants, or got higher. For example, in the case of RS with $k = 1$, the error is 26 meV higher. For all non-cubic systems, improvements are achieved. Their improvements could be caused by the fact, that in the case of lattice constants, the performances are lower due to the constraint by the multi-task problem. As mentioned before, building separate models for each lattice constant, is not considered in the frame of this work.

E_{Mad}, given by the *direct* fits, is included in the feature space now ($\mathcal{C}_3(F_{\mathrm{Mad}})$), from which models are built to describe the energy differences. This is done for different dimensions $k_{E_{\mathrm{Mad}}}$ of the input models, representing the different degrees of error (see Fig. 5.8). The resulting RMSE of the final models $f_{\Delta E}$ are not significantly different to the RMSE of models with E_{Mad} from the DFT geometries (case X). The new found descriptors and the descriptors of the models from X, only coincide for low dimensions of $k_{\Delta E}$. For $k_{E_{\mathrm{Mad}}} = 5$ (smaller error), the descriptors of $k_{\Delta E} = 1$ and $k_{\Delta E} = 2$ coincide with the corresponding ones from case X. For $k_{E_{\mathrm{Mad}}} = 1$ (higher error), only the descriptor of $k_{\Delta E} = 1$ coincide with the one from case X.

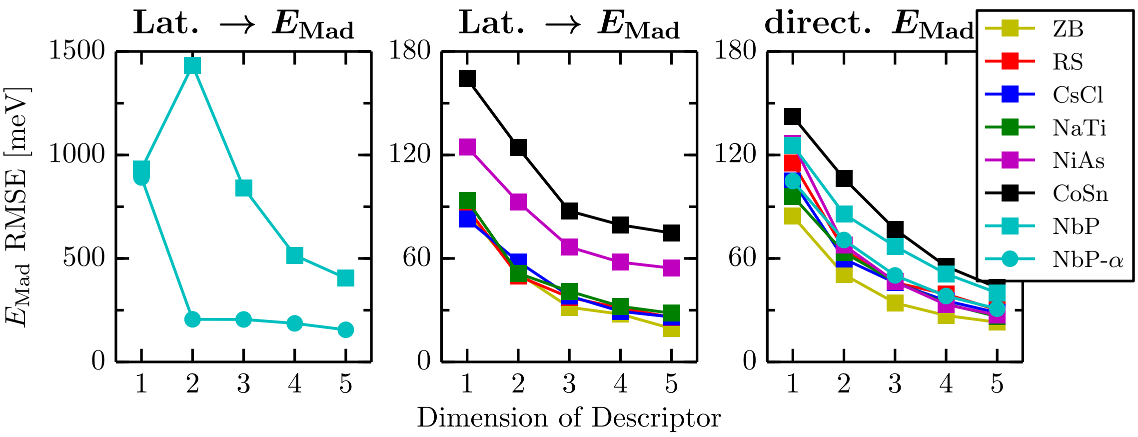

Figure 5.7: RMSE for models to describe the the Madelung energy E_{Mad}. On the left and in the center, the errors for E_{Mad}, calculated from models, built to describe the lattice constants, are represented. On the right, the errors, built to describe E_{Mad} directly, are shown.

5.6.3 Prediction for F_{19}

Five times 10-fold-cross-validation was performed for four different sets of considered structures in the multi-task problem[7]. The used feature space is $\mathcal{C}_3(F_{19})$. The sets are defined, as in the following:

$$\begin{aligned}
S_1 &= \{\text{RS, CsCl, NaTi, NiAs, CoSn, NbP, CrB}\}\\
S_2 &= \{\text{RS, CsCl, NaTi, NiAs, CoSn, NbP}\qquad\}\\
S_3 &= \{\text{RS, CsCl, NaTi, NiAs, CoSn,}\qquad\text{CrB}\}\\
S_4 &= \{\text{RS, CsCl,}\qquad\text{NiAs,}\qquad\qquad\text{CrB}\}.
\end{aligned}$$

As described in Sec. 3.8, in each of the ten cross-validation iterations, for all structures, the same materials are considered in the training/test. The descriptors are obtained from the test set for a given S_i. With the different coefficients for different structures, predictions are evaluated on the materials of the test set for only the same structures (of S_i).

The obtained results are shown in 5.9. The prediction errors are higher than the errors from fitting all 82 materials (Fig. 5.4), varying from 80 meV (S_4, CrB) to 854 meV (S_2, NbP). Still, the structures CsCl, NaTi, and NbP give the highest errors. As mentioned before the energy differences of CsCl and NaTi, show relatively high standard deviations. The highest RMSE/σ ratio is given by NbP. For the remaining structures with $2 \leq k \leq 4$, in general, errors around 100 meV are achieved. The performance of these cases, do not depend significantly on the used set of structures. In opposition to the fitting errors (Fig. 5.4), in the cases S_2, S_3 and S_4, the averaged error does not increase with each higher dimension k (overfitting). In contrast, when including all structures (S_1), a convergence behaviour is observed, for the considered k-values.

---

[7] Note, that the cross-validation is applied for all sets separately. The purpose is, to analyse the contribution of the included structures to the prediction performance of the obtained model.

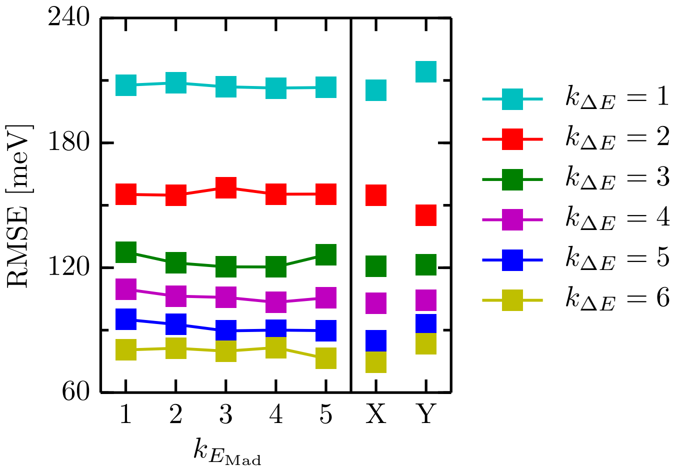

Figure 5.8: Influence of the errors of $k_{E_{\text{Mad}}}$, on models $f_{\Delta E}$, built to describe the energy differences. The quadratic mean over the RMSE of all relative stabilities is represented. The final models are obtained from $\mathcal{C}_3(F_{\text{Mad}})$, for different $k_{\Delta E}$. The used E_{Mad} is obtained from fits $f_{E_{\text{Mad}}}$. The influence is considered for different dimension $k_{E_{\text{Mad}}}$ of $f_{E_{\text{Mad}}}$. The errors of the models $f_{E_{\text{Mad}}}$ are shown in Fig. 5.7. X stands for the models $f_{\Delta E}$, where E_{Mad} is obtained from the DFT geometries (red line in Fig. 5.5). Y represents models obtained from $\mathcal{C}_3(F_{19})$ (purple line in Fig. 5.5)

The predicted energy differences $\Delta E_{\text{predict}}$ for S_2 and CsCl, as an example of overfitting, are shown in Fig. 5.10. The increase of the error for $k = 5$ is not caused, by all 82 materials, but by BN. The RMSE (prediction error) for the remaining materials is in the case $k = 2$ lower than in the case $k = 5$. For excluded BN, $\text{RMSE}_{k=2} = 172$ meV and $\text{RMSE}_{k=5} = 117$ meV. Note, that for exluded BN and CC, $\text{RMSE}_{k=5} = 100$ meV.

A similar behaviour is observed for S_1 and NbP, where now the dimension of overfitting is lower. The highest errors are again achieved by BN and C. For excluded BN and C, $\text{RMSE}_{k=2} = 161$ meV and $\text{RMSE}_{k=5} = 96$ meV. Moreover, the build models underestimate high energy differences (except BN and C) and tend to overestimate low energy differences. This characteristic is reduced by the 5-dimensional model.

The highest errors are not for all cases given by C and BN. However, C exhibits most frequently the highest error, showing also most frequently the highest outlying energy difference[8].

A way to reduce the large errors could be given by building more than one model on the training set, i.e., local rather than global models. The idea is that, for different materials, different physical quantities could dominate, when describing different energy differences. A technique called sub-group discovery [24] has been recently applied [25] to successfully classify rocksalt and zincblende materials, for the usual set of 82 octet binaries, by means of

---

[8] For all differences relative to ZB, diamond shows the highest energy difference, except for NbP. Also for differences not relative to ZB, C exhibits the highest or relatively high values for several cases.

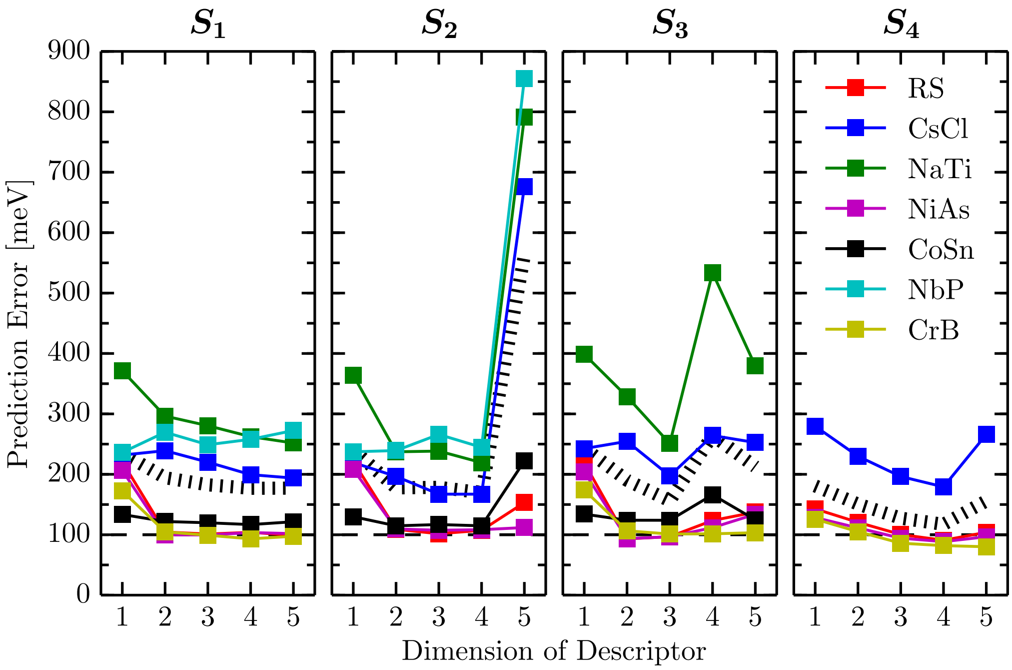

Figure 5.9: Prediction Error for multi task models for the four sets S_1, S_2, S_3 and S_4 of structures. The used feature space is $\mathcal{C}_3(F_{19})$. For each set, five times 10-fold-cross-validation is performed. The dotted line represents the quadratic mean over the RMSE of all relative stabilities.

simple boolean statements about the atomic properties of the constituents. This technique can be modified in order to discover sub-groups where the SIS$-\ell_0$ model is locally optimal. Work in this direction is currently in progress.

However, from the analysis on fitting all 82 materials (Fig. 5.4), we know that there exist models, which can describe all 82 materials accurately. Obviously, the prediction performances suffer from the small set of materials, e.g. that materials, which are *similar* to the outliers, are not contained in the training set. Out of the frame of this work, also a leave-1-out-cross validation is needed, in which the model is built on the 81 Materials and the remaining one is predicted, to judge if with the 81 materials enough information is obtained to describe also the outliers.

Furthermore, the effect of including all the eight Madelung energies directly into the feature space has to be tested. It was shown, that different models achieve similar good results in fitting the energy differences, as with F_{19} and F_{Mad} similar fitting performances are obtained. Nevertheless when one *good* model can show an overfitting behaviour, the other good model could show reasonable prediction performances.

As seen in Fig. 5.9, the overfitting behaviour is observed rather for higher k-values. A not addressed issue in this work, is the dependency of the prediction on the complexity of the features, as a product of $\mathcal{C}_i$. In Sec. 5.3, it was shown that, already with $\mathcal{C}_2$ errors around 50 meV are achieved for separate models on the RS-ZB case. It has to be investigated,

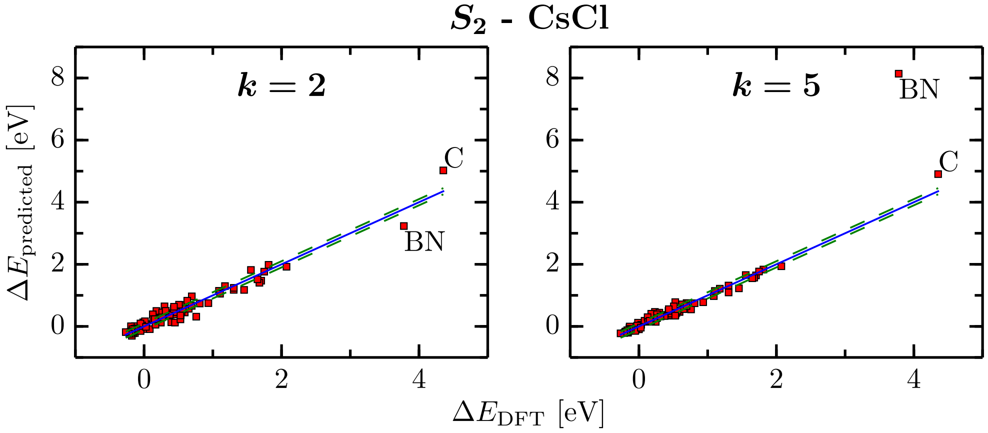

Figure 5.10: Predicted energy differences $\Delta E_{\text{predict}}$ vs. DFT energy differences ΔE_{DFT}, for models to describe CsCl-ZB. The models are obtained by a multi-task problem with the set S_1 and $\mathcal{C}_3(F_{19})$. The RMSE is presented in 5.9

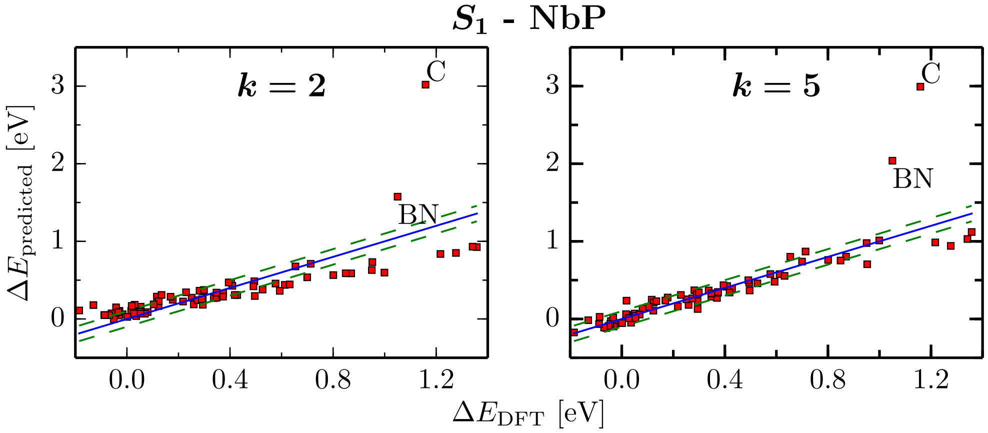

Figure 5.11: Predicted energy differences $\Delta E_{\text{predict}}$ vs. DFT energy differences ΔE_{DFT}, for models to describe NbP-ZB. The models are obtained by a multi-task problem with the set S_2 and $\mathcal{C}_3(F_{19})$. The RMSE is presented in 5.9

how a multi task problems perform in fitting and predicting with $\mathcal{C}_2$, and how much and if improvements are gained in predicting with $\mathcal{C}_3$. In addition, the prediction performance of the separate models has to be compared with the one of the multi-task models, to investigate if improvements are obtained in prediction by multi-task models although they show worse training errors, e.g. if a multi-task problem contributes in the sense, that the size of the set of materials (samples) is increased, and thus more information is obtained in the resulting model.

What we learn from the prediction results is, that with $k = 2$ and $k = 3$ good estimates are obtained and the risk of overfitting is smaller than for higher k-values, thus better suitable for prediction. Hence, to build a model for prediction, cross-validation could be used to determine the optimal k. A promising model would then be built on all 82 materials for $k = 3$.

The cross-validation as presented in this work evaluates the performance of the idea of using the best obtained fit for prediction. As seen, this can lead to low prediction performances in some case. Thus a models should be built in a smarter way, such as by different cross-validation techniques and taking also other quantities besides the RMSE into consideration.

6 Conclusions

In this work, we have addressed the challenge of predicting the ground-state and metastable crystal structures of materials, by knowing just their composition and physical information on the atomic species building them. This is perhaps the most fundamental and important challenge in materials science. We have focused on a class of binary semiconductor with eight valence electrons per unit cell, the so called octet binaries, and we have applied a recently developed statistical-learning method, inspired by the work presented in Ghiringhelli *et al.*, Phys. Rev. Lett. **114**, 105503 (2015). The improved method allows for the discovery of a predicting model out of more than 10^{10} candidates to describe the relative (meta-)stability of the octet binary compounds. Each candidate model is built as a non-linear function of *primary features*, i.e., physical properties (Kohn-Sham levels, radial extension of the valence orbitals, etc.) of the gas-phase atomic species building the material. The eight crystal structures zincblende, rocksalt, CsCl, NiAs, NaTi, CoSn, NbP, and CrB were considered for 82 octet binary compounds.

For all materials and crystal structures, the accurate energy of the relaxed (local minimum) geometry was calculated, within the work of this thesis, by using the density-functional theory within the local-density approximation (LDA). The structures NiAs, CoSn, NbP, CrB have proven to be more complex than the original cubic structures from Ghiringhelli *et al.*'s work, leading to multiple minima, therefore requiring extensive scan of the potential energy surfaces and a careful analysis.

With respect to the statistical-learning compressed-sensing based scheme introduced in Ghiringhelli *et al.*'s work, the new compressed-sensing scheme applied in this thesis, mainly developed by Runhai Ouyang and Luca Ghiringhelli in the group of Prof. Matthias Scheffler, overcomes the limitation to few thousands of candidate models (the feature space), by allowing feature spaces of billions to trillions features (models). New primary features were introduced in this work, from the more obvious atomic and valence-electron numbers, through non-atomic features such as dimer formation energy, equilibrium distance, to *a representative of a novel class of features* that express the basic geometrical information of the various crystal structures. The introduction of a feature that maps the complex, multidimensional information into a well defined scalar, here in the form of a reduced Madelung energy, requires the definition of a two-steps approach. First, the geometrical parameters are predicted from the "pure" atomic (and dimer) properties, then the Madelung energy is evaluated and used as primary feature alongside with the others. Moreover, a new multi-task concept was introduced: finding a descriptor capable of describing several energy differences simultaneously. With excluded Madelung energy, such a descriptor

could describe the relative stabilities with an average error below below 0.1 eV. Further improvements were obtained by adding the Madelung energy.
The work was concluded with an outlook, providing a motivation and basis for smartly designed techniques to overcome difficulties in predicting new materials.

A Descriptors

In the following, the descriptors of a multi-task model built from F_{19} and by using all 82 data points are represented for different dimensions k of descriptor:

$k = 1:$

$$|\mathrm{EA(A)} - \mathrm{HOMO(B)}| \cdot \frac{N_{\mathrm{val}}(\mathrm{B})}{N_{\mathrm{val}}(\mathrm{A})} \cdot \frac{e^{\mathrm{EA(B)}}}{|r_s(\mathrm{B}) - d_{\mathrm{dim}}|}$$

$k = 2:$

$$|\mathrm{EA(A)} - \mathrm{HOMO(B)}| \cdot \frac{N_{\mathrm{val}}(\mathrm{B})}{N_{\mathrm{val}}(\mathrm{A})} \cdot \frac{e^{\mathrm{EA(B)}}}{|r_s(\mathrm{B}) - d_{\mathrm{dim}}|},$$
$$\frac{||r_p(\mathrm{A}) - d_{\mathrm{dim}}| - r_p(\mathrm{A})|}{|\frac{r_p(\mathrm{A})}{N(\mathrm{B})} - \frac{d_{\mathrm{dim}}}{N_{\mathrm{val}}(\mathrm{A})}|}$$

$k = 3:$

$$|\mathrm{EA(A)} - \mathrm{HOMO(B)}| \cdot \frac{N_{\mathrm{val}}(\mathrm{B})}{N_{\mathrm{val}}(\mathrm{A})} \cdot \frac{e^{\mathrm{EA(B)}}}{|r_s(\mathrm{B}) - d_{\mathrm{dim}}|},$$
$$\frac{||r_p(\mathrm{A}) - d_{\mathrm{dim}}| - r_p(\mathrm{A})|}{|\frac{r_p(\mathrm{A})}{N(\mathrm{B})} - \frac{d_{\mathrm{dim}}}{N_{\mathrm{val}}(\mathrm{A})}|},$$
$$|\frac{\mathrm{EA(A)} \cdot r_p(\mathrm{A})}{\mathrm{EA(B)} \cdot r_p(\mathrm{B})} - |\frac{\mathrm{HOMO(A)}}{\mathrm{EA(A)}} - e^{r_s(\mathrm{B})}||$$

$k = 4:$

$$|\mathrm{EA(A)} - \mathrm{HOMO(B)}| \cdot \frac{N_{\mathrm{val}}(\mathrm{B})}{N_{\mathrm{val}}(\mathrm{A})} \cdot \frac{e^{\mathrm{EA(B)}}}{|r_s(\mathrm{B}) - d_{\mathrm{dim}}|},$$
$$\frac{||r_p(\mathrm{A}) - d_{\mathrm{dim}}| - r_p(\mathrm{A})|}{|\frac{r_p(\mathrm{A})}{N(\mathrm{B})} - \frac{d_{\mathrm{dim}}}{N_{\mathrm{val}}(\mathrm{A})}|},$$
$$|\frac{\mathrm{EA(A)}}{|\mathrm{EA(A)} - \mathrm{HOMO(A)}|} - \frac{N_{\mathrm{val}}(A)}{\mathrm{EA(B)}} \cdot \frac{\mathrm{LUMO(B)}}{N(\mathrm{A})}|,$$
$$|\frac{\mathrm{EA(A)} \cdot r_s(\mathrm{A})}{\mathrm{EA(B)} \cdot r_s(\mathrm{B})} - |\frac{\mathrm{HOMO(A)}}{\mathrm{EA(B)}} - e^{r_s(\mathrm{B})}||$$

$k = 5:$

$$|\mathrm{EA(A)} - \mathrm{HOMO(B)}| \cdot \frac{N_{\mathrm{val}}(\mathrm{B})}{N_{\mathrm{val}}(\mathrm{A})} \cdot \frac{e^{\mathrm{EA(B)}}}{|r_s(\mathrm{B}) - d_{\mathrm{dim}}|},$$

$$||r_p(\mathrm{A}) - d_{\mathrm{dim}}| - r_p(\mathrm{A})| \cdot \frac{N_{\mathrm{val}}(\mathrm{A})}{e^{d_{\mathrm{dim}}}},$$

$$\frac{\frac{\mathrm{LUMO(B)}}{\mathrm{EA(B)}} + \frac{N(\mathrm{A})}{N_{\mathrm{val}}(B)}}{(\mathrm{EA(A)} + \mathrm{EA(B)}) \cdot d_{\mathrm{dim}} \cdot N(\mathrm{A})},$$

$$\frac{N(\mathrm{B})}{\mathrm{IP(A)}} \cdot \frac{\mathrm{LUMO(A)}}{N_{\mathrm{val}}(\mathrm{A})} + |\frac{\mathrm{HOMO(A)}}{\mathrm{EA(A)}} - e^{r_s(\mathrm{A})}|,$$

$$|\frac{\mathrm{EA(A)} \cdot r_p(\mathrm{A})}{\mathrm{EA(B)} \cdot r_p(\mathrm{B})} - |\frac{\mathrm{HOMO(A)}}{\mathrm{EA(B)}} - e^{r_s(B)}||$$

$k = 6:$

$$|\mathrm{EA(A)} - \mathrm{HOMO(B)}| \cdot \frac{N_{\mathrm{val}}(\mathrm{B})}{N_{\mathrm{val}}(\mathrm{A})} \cdot \frac{e^{\mathrm{EA(B)}}}{|r_s(\mathrm{B}) - d_{\mathrm{dim}}|} \qquad ,$$

$$\frac{||r_p(\mathrm{A}) - d_{\mathrm{dim}}| - r_p(\mathrm{A})|}{|\frac{r_p(\mathrm{A})}{N(\mathrm{B})} - \frac{d_{\mathrm{dim}}}{N_{\mathrm{val}}(\mathrm{A})}|},$$

$$\frac{\frac{\mathrm{LUMO(B)}}{\mathrm{EA(B)}} + \frac{N(\mathrm{A})}{N_{\mathrm{val}}(A)}}{\mathrm{EA(A)} + \mathrm{EA(B)} \cdot d_{\mathrm{dim}} \cdot N(\mathrm{A})},$$

$$|\frac{\mathrm{EA(A)} \cdot r_s(\mathrm{A})}{\mathrm{EA(B)} \cdot r_s(\mathrm{B})} - |\frac{\mathrm{HOMO(A)}}{\mathrm{EA(B)}} - e^{r_s(\mathrm{B})}||,$$

$$\frac{\frac{N(\mathrm{A}) + N_{\mathrm{val}}(A)}{|\mathrm{HOMO(A)\text{-}LUMO(B)}|}}{|N(\mathrm{A}) - N_{\mathrm{val}}(A)| + |N(\mathrm{B}) - N_{\mathrm{val}}(\mathrm{A}))|},$$

$$|\frac{\mathrm{EA(A)}}{d_{\mathrm{dim}}} + \frac{\mathrm{LUMO(B)}}{r_{\mathrm{p}}(B)} - |\frac{\mathrm{EA(B)} - \mathrm{LUMO(B)}}{r_{\mathrm{p}}(A)}||$$

In the following, the descriptors of a multi-task model built from F_{Mad} and by using all 82 data points are represented for different dimensions k of descriptor:

$k = 1:$

$$|\frac{E^{\mathrm{X}}_{\mathrm{Mad}}}{e^{d_{\mathrm{dim}}} \cdot r_{\mathrm{p}}} - \frac{E^{\mathrm{ZB}}_{\mathrm{Mad}} \cdot r_s(\mathrm{B})}{r_p(\mathrm{B}) \cdot d_{\mathrm{sim}}}|$$

$k = 2:$

$$\frac{\mathrm{IP(B)} \cdot N^4_{\mathrm{val}}(\mathrm{B}) \cdot e^{\mathrm{EA(B)}}}{r_s(\mathrm{B}) - d_{\mathrm{dim}}},$$

$$||E^{\mathrm{X}}_{\mathrm{Mad}} - \mathrm{EA(B)}| \cdot |r_s(\mathrm{A}) - r_s(\mathrm{B})|| - \frac{\mathrm{EA}(B) r_s^2(\mathrm{B})}{d_{\mathrm{dim}}}$$

$$k = 3:$$

$$|\mathrm{EA(A)\text{-}HOMO(B)}| \cdot \frac{N_{\mathrm{val}}(\mathrm{B})}{N_{\mathrm{val}}(\mathrm{B})},$$

$$|\frac{\mathrm{HOMO(B)}}{E^{\mathrm{ZB}}_{\mathrm{MAD}}} - \frac{r_s(\mathrm{A})}{d_{\mathrm{dim}} \cdot |E^{\mathrm{X}}_{\mathrm{Mad}} - \mathrm{EA(B)}| + \mathrm{EA(A)} + HOMO(B)}|,$$

$$\frac{|E^{\mathrm{X}}_{\mathrm{Mad}} - EA(\mathrm{B})|}{E^{\mathrm{X}}_{\mathrm{Mad}} - EA(\mathrm{A})} \cdot ||r_p(\mathrm{A}) - d_{\mathrm{dim}}| - r_s(\mathrm{A})|$$

$$k = 4:$$

$$|\frac{E^{\mathrm{X}}_{\mathrm{Mad}}}{r_p(\mathrm{B}) e^{d_{\mathrm{dim}}}} - \frac{E^{\mathrm{ZB}}_{\mathrm{Mad}} \cdot r_s(\mathrm{B})}{r_p(\mathrm{B}) \cdot d_{\mathrm{dim}}}|,$$

$$\frac{\mathrm{IP(B)} \cdot N^3_{\mathrm{val}}(B) \cdot e^{\mathrm{EA(B)}}}{|r_s(\mathrm{B}) - d_{\mathrm{dim}}|},$$

$$\frac{\frac{|\mathrm{HOMO(B)}|}{E^{\mathrm{ZB}}_{\mathrm{Mad}}} - \frac{r_s(\mathrm{A})}{d_{\mathrm{dim}}}}{|E^{\mathrm{X}}_{\mathrm{Mad}} - \mathrm{EA(B)}{+}\mathrm{EA(A)}{+}\mathrm{HOMO(B)}|},$$

$$\frac{|E^{\mathrm{X}}_{\mathrm{Mad}} - \mathrm{EA(B)}| \cdot ||r_p(\mathrm{A} - d_{\mathrm{dim}})| - r_s(\mathrm{A})|}{E^{\mathrm{X}}_{\mathrm{Mad}} + \mathrm{EA(A)}}$$

$$k = 5:$$

$$(E^{\mathrm{ZB}}_{\mathrm{Mad}} \cdot \mathrm{HOMO(B)})^3 \cdot e^{\mathrm{HOMO(B)}} \cdot \mathrm{HOMO(B)}^3,$$

$$\frac{E^{\mathrm{X}}_{\mathrm{Mad}} |r_s(\mathrm{A} - d_{\mathrm{dim}})|}{r_s(\mathrm{A})} + \frac{\mathrm{EA(A)} \cdot \mathrm{HOMO(B)}}{\mathrm{HOMO(A)}{+}\mathrm{LUMO(B)}},$$

$$|\frac{E^{\mathrm{ZB}}_{\mathrm{Mad}}}{\mathrm{IP(B)}} + \frac{N_{\mathrm{val}}(\mathrm{A})}{N_{\mathrm{val}}(\mathrm{B})} - \frac{\mathrm{IP(A)}{+}\mathrm{HOMO(B)}}{|\mathrm{IP(B)\text{-}HOMO(A)}|},$$

$$\sqrt{|E^{\mathrm{X}}_{\mathrm{Mad}} - E^{\mathrm{ZB}}_{\mathrm{Mad}}| \cdot |E^{X}_{\mathrm{Mad}} - \mathrm{EA(A)}| \cdot \frac{N_{\mathrm{val}}(A)}{d_{\mathrm{dim}}}},$$

$$|\frac{\mathrm{HOMO(B)}}{E^{\mathrm{ZB}}_{\mathrm{Mad}}}| - \frac{r_s(\mathrm{A})}{|E^{\mathrm{X}}_{\mathrm{Mad}} - \mathrm{EA(A)}|} + \mathrm{EA(B)}{+}\mathrm{HOMO(B)}$$

$$k = 6:$$

$$(E^{\mathrm{ZB}}_{\mathrm{Mad}} \cdot \mathrm{HOMO(B)})^3 \cdot e^{\mathrm{HOMO(B)}} \cdot \mathrm{HOMO(B)}^3,$$

$$\frac{E^{\mathrm{X}}_{\mathrm{Mad}} |r_s(\mathrm{A} - d_{\mathrm{dim}})|}{r_s(\mathrm{A})} + \frac{\mathrm{EA(A)} \cdot \mathrm{HOMO(B)}}{\mathrm{HOMO(A)}{+}\mathrm{LUMO(B)}},$$

$$|\frac{E^{\mathrm{ZB}}_{\mathrm{Mad}}}{\mathrm{IP(B)}} + \frac{N_{\mathrm{val}}(\mathrm{A})}{N_{\mathrm{val}}(\mathrm{B})} - \frac{\mathrm{IP(A)}{+}\mathrm{HOMO(B)}}{|\mathrm{IP(B)\text{-}HOMO(A)}|},$$

$$\sqrt{|E^{\mathrm{X}}_{\mathrm{Mad}} - E^{\mathrm{ZB}}_{\mathrm{Mad}}| \cdot |E^{X}_{\mathrm{Mad}} - \mathrm{EA(A)}| \cdot \frac{N_{\mathrm{val}}(A)}{d_{\mathrm{dim}}}},$$

$$|\frac{\mathrm{LUMO(B)}}{\mathrm{IP(B)}} + \frac{\mathrm{EA(A)}}{\mathrm{HOMO(A)}} - \frac{|r_d(\mathrm{A}) - d_{\mathrm{dim}}|}{r_d(\mathrm{A}) + d_{\mathrm{dim}}}|,$$

$$|\frac{\mathrm{HOMO(B)}}{E^{ZB}_{\mathrm{Mad}}} - \frac{r_s(\mathrm{A})}{d_{\mathrm{dim}} \cdot |E^{\mathrm{X}}_{\mathrm{Mad}} - \mathrm{EA(A)}| + \mathrm{EA(B)}{+}\mathrm{HOMO(B)}}|$$

B Materials and details about the crystal structures

The used 82 materials are listed in the following:
LiF, LiCl, LiBr, LiI, NaF, NaCl, NaBr, NaI, KF, KCl, KBr, KI, RbF, RbCl, RbBr, RbI, CsF, CsCl, CsBr, CsI, AgF, AgCl, AgBr, AgI, CuF, CuCl, CuBr, CuI, BeO, BeS, BeSe, BeTe, MgO, MgS, MgSe, MgTe, CaO, CaS, CaSe, CaTe, SrO, SrS, SrSe, SrTe, BaO, BaS, BaSe, BaTe, ZnO, ZnS, ZnSe, ZnTe, CdO, CdS, CdSe, CdTe, BN, BP, BAs, BSb, AlN, AlP, AlAs, AlSb, GaN, GaP, GaAs, GaSb, InN, InP, InAs, InSb, SnSn, SnGe, SnSi, SnC, GeGe, GeSi, GeC, SiSi, SiC, CC.

Details about the unit cell and atomic coordinates of the used crystal structures are represented in the following table [19]:

crystal structure	lattice vectors	atomic coordinates	
RS	$\begin{matrix} 0 & a/2 & a/2 \\ a/2 & 0 & a/2 \\ a/2 & a/2 & 0 \end{matrix}$	$\begin{matrix} 0 & 0 & 0 \\ 1/2 & 1/2 & 1/2 \end{matrix}$	A B
ZB	$\begin{matrix} 0 & a/2 & a/2 \\ a/2 & 0 & a/2 \\ a/2 & a/2 & 0 \end{matrix}$	$\begin{matrix} 0 & 0 & 0 \\ 1/4 & 1/4 & 1/4 \end{matrix}$	A B
CsCl	$\begin{matrix} a & 0 & 0 \\ 0 & a & 0 \\ 0 & 0 & a \end{matrix}$	$\begin{matrix} 0 & 0 & 0 \\ 1/2 & 1/2 & 1/2 \end{matrix}$	A B
NaTi	$\begin{matrix} 0 & a/2 & a/2 \\ a/2 & 0 & a/2 \\ a/2 & a/2 & 0 \end{matrix}$	$\begin{matrix} 1/8 & 1/8 & 1/8 \\ -1/8 & -1/8 & -1/8 \\ 3/8 & 3/8 & 3/8 \\ -3/8 & -3/8 & -3/8 \end{matrix}$	A A B B
NiAs	$\begin{matrix} a/2 & -\sqrt{3}\ a/2 & 0 \\ a/2 & \sqrt{3}a/2 & 0 \\ 0 & 0 & c \end{matrix}$	$\begin{matrix} 0 & 0 & 0 \\ 0 & 0 & 1/2 \\ 1/3 & 2/3 & 1/4 \\ 2/3 & 1/3 & 3/4 \end{matrix}$	A A B B
CoSn	$\begin{matrix} a/2 & -\sqrt{3}\ a/2 & 0 \\ a/2 & \sqrt{3}a/2 & 0 \\ 0 & 0 & c \end{matrix}$	$\begin{matrix} 0 & 0 & 0 \\ 1/3 & 2/3 & 1/2 \\ 2/3 & 1/3 & 1/2 \\ 1/2 & 0 & 0 \\ 0 & 1/2 & 0 \\ 1/2 & 1/2 & 0 \end{matrix}$	A A A B B B
NbP	$\begin{matrix} a & 0 & 0 \\ 0 & a & 0 \\ a/2 & a/2 & d/2 \end{matrix}$	$\begin{matrix} -1/8 & 5/8 & 1/4 \\ 1/8 & -5/8 & -1/4 \\ -3/8 & -1/8 & 3/4 \\ 3/8 & 2/8 & -3/4 \end{matrix}$	A A B B
CrB	$\begin{matrix} a/2 & -\ b/2 & 0 \\ a/2 & b/2 & 0 \\ 0 & 0 & c \end{matrix}$	$\begin{matrix} -u & u & 1/4 \\ u & -u & 3/4 \\ -v & v & 1/4 \\ v & -v & 3/4 \end{matrix}$	A A B B

C Convergence tests

In this chapter several convergence tests are demonstrated. All energies are given in the unit per atom.

C.1 Birch-Murnaghan-fit

In Fig. C.1, the influence of the range of a BM-fit on the obtained equilibrium energy is represented. For the tests, RS, ZB, CsCl and NiAs is considered. A 4%-range was chosen. With smaller ranges, the risk increases, that lattice constants found with light setting, could lie out of the range for tight settings and third tier basis set. For the not considered structures, which depend on 2 parameters, also the range of the second parameter has to be checked when building a range of 4% for a, e.g. a 4%-range for a leads for some materials NbP structure to d-ranges above 10% in the .

C.2 k-grid

The dependence of the energy on the Gaussian broadening width is demonstrated in Fig. C.2. Here the converged energies with respect to the k-grid (below 0.5 meV) are plotted vs. the width.

In Fig. C.3 they k-grid test is presented, where the k-points are varied along one lattice vector and is fixed for the others. From the tests, a ratio between k_a and k_c is determined, see 4.2.

The k-grid convergence tests are demonstrated in Fig. C.4 for energies, and in Fig. C.5 and Fig. C.6. In the NbP-α case, in general a converged k-grid wit $20 \times 20 \times 20$ is used. There are some exceptions which show a high sensitivity on the k-grid, such as SiSi, GeC, GeGe, GeSi, InSb, SnC, SnGe and SnSn. For these exceptions $40 \times 40 \times 40$ k-points are used.

C.3 Integration grid

The test on the integration grid was done with converged a k-grid (see 4.2) and default tier basis set. For the tests (see Fig. C.7), the structures RS, ZB, CsCl and NiAs are considered. The different structures give similar pictures, e.g. a low dependency of the convergence of

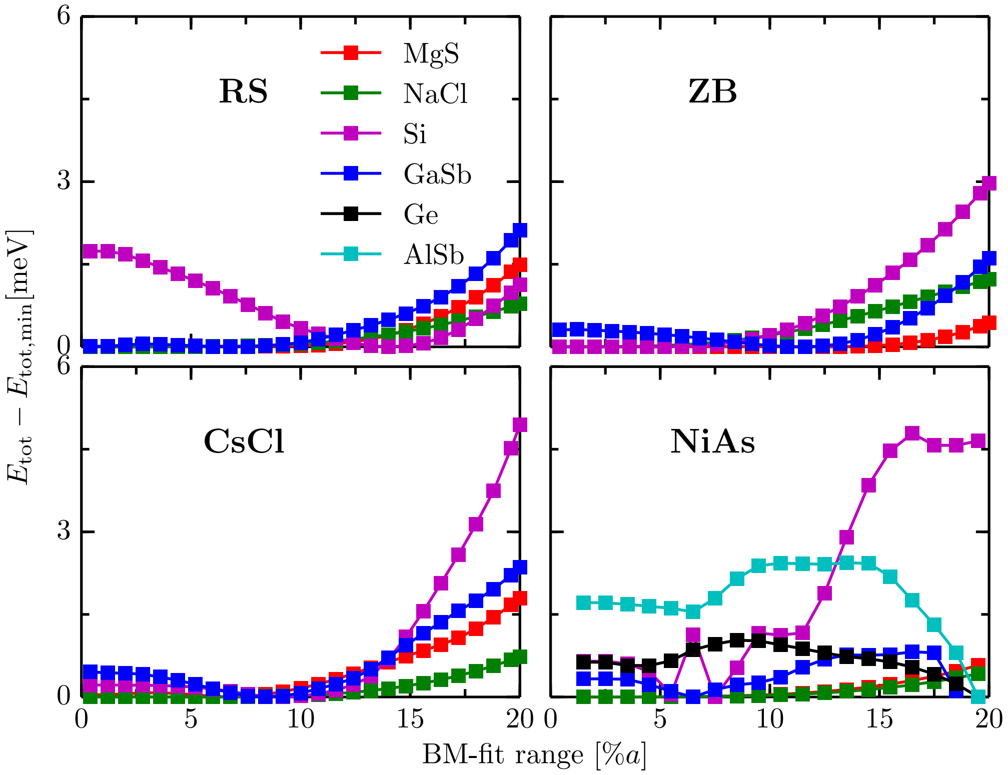

Figure C.1: The dependence of the equilibrium energy from a 5-point BM-fit on its range. For the 5 points within $\tilde{a} \pm \frac{\gamma}{100}\tilde{a}$, the range is defined to be $2 \cdot \gamma\%$. $\tilde{a}$ is a start value close to the equilibrium a_0. For the cubic systems systems, light settings and $8 \times 8 \times 8$ k-points are used, for the NiAs structure tight settings and the converged k-grid (see Tab.4.2) with a k-point density of 12.2 and 25.4 for $\boldsymbol{a}^*$ and $\boldsymbol{b}^*$

the integration grids on the structures is observed. The dependence of the lattice constants on the integration grid is demonstrated in Fig. C.8.

C.4 Basis set

The tests with respect to the basis set is done with a converged k-grid (see 4.2) and tight settings. The tests for the energies are shown in Fig. C.9 and for the lattice constants in Fig. C.10.

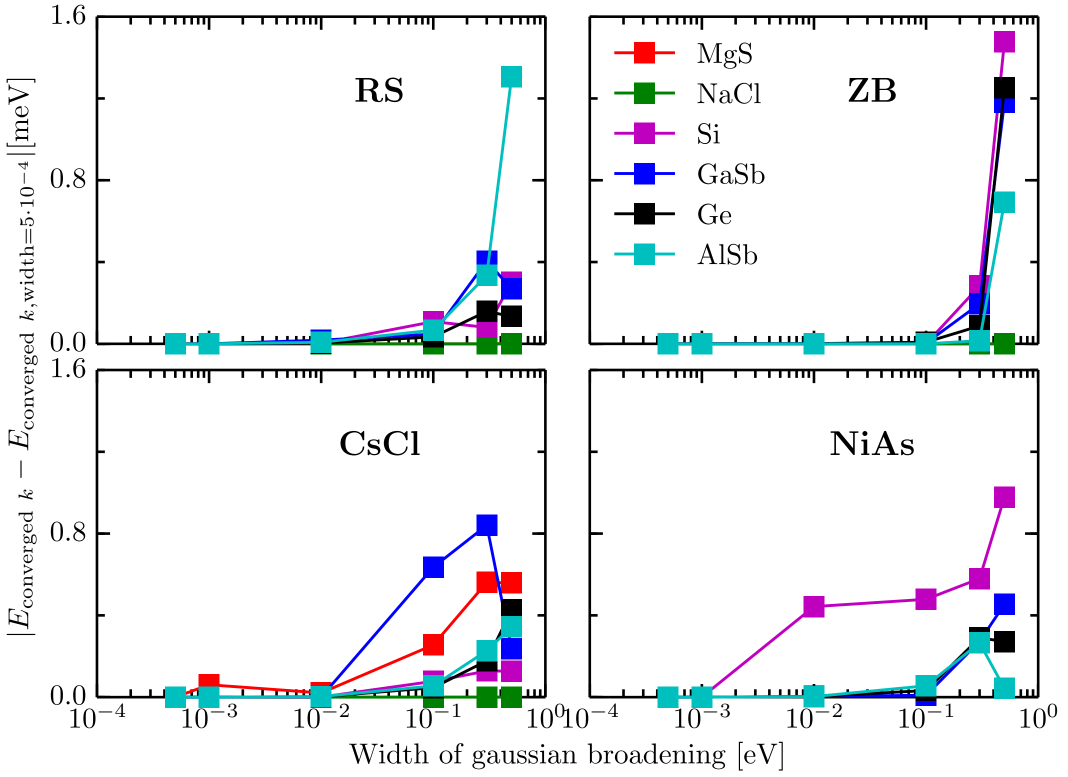

Figure C.2: Dependence of the energy on the Gaussian broadening width. For each considered width the k-grid is converged below 0.5 meV. (5-8)-point BM-fits with a 2%-range are used.

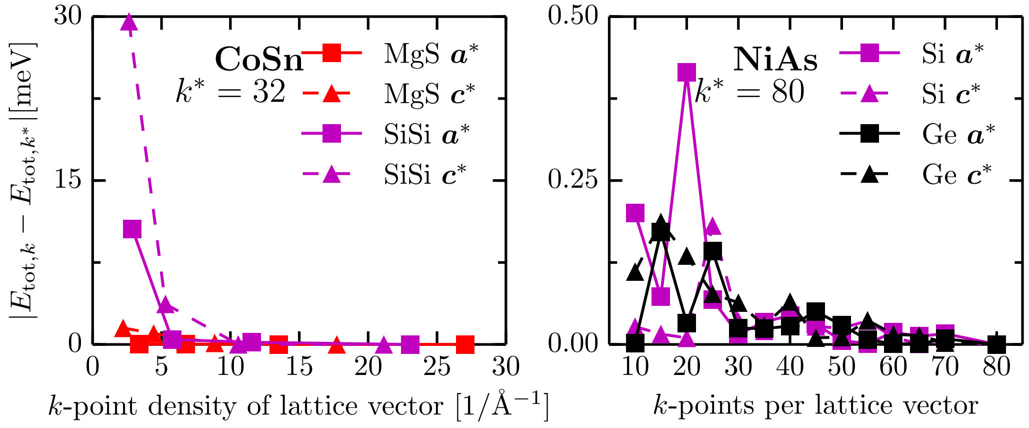

Figure C.3: Dependence of the convergence with respect to the k-points along the lattice vectors a^* and c^*. (5-8)-point BM-fits with a 2%-range are used.

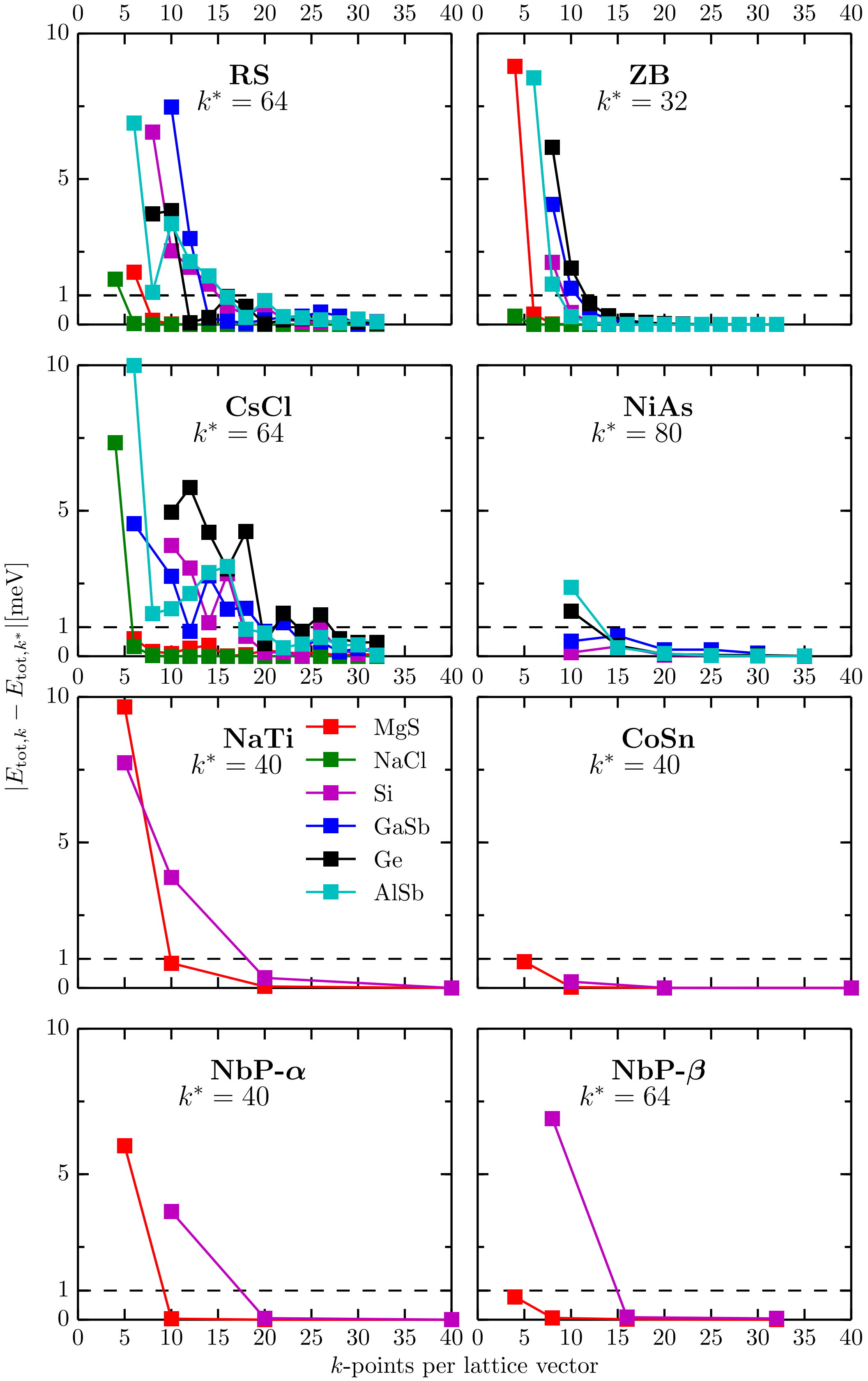

Figure C.4: k-grid convergence test for total energies. (5-8)-point BM-fits with a 2%-range are used.

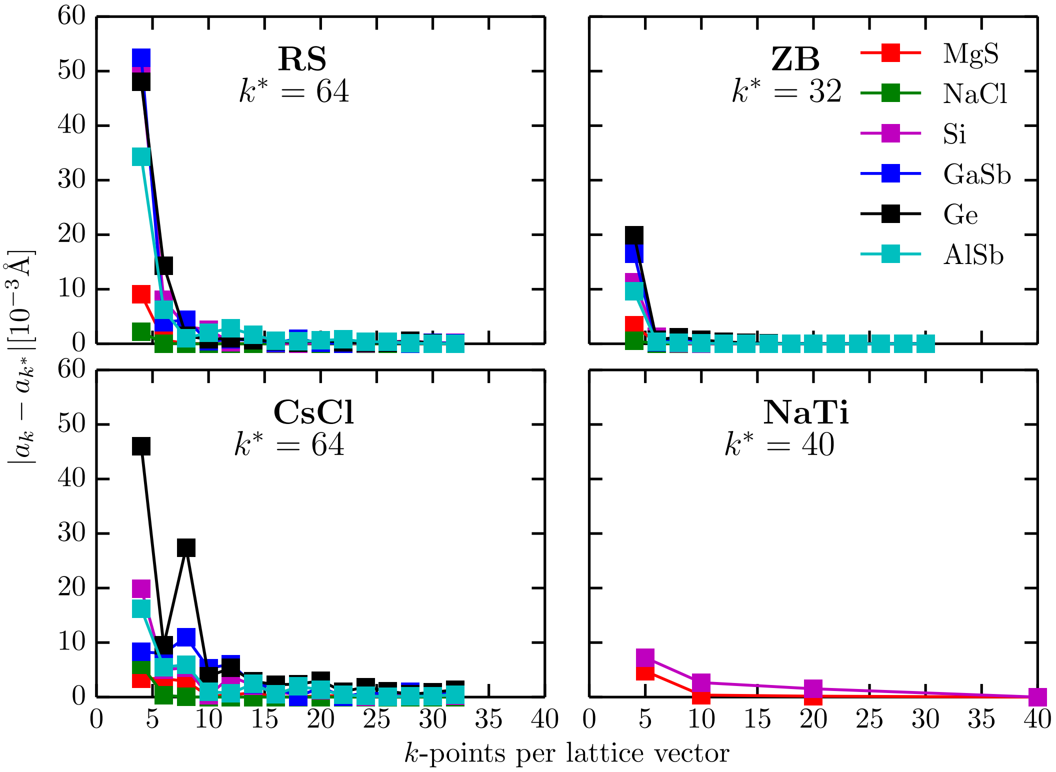

Figure C.5: k-grid convergence test for lattice constant a of the cubic systems (5-8)-point BM-fits with a 2%-range are used.

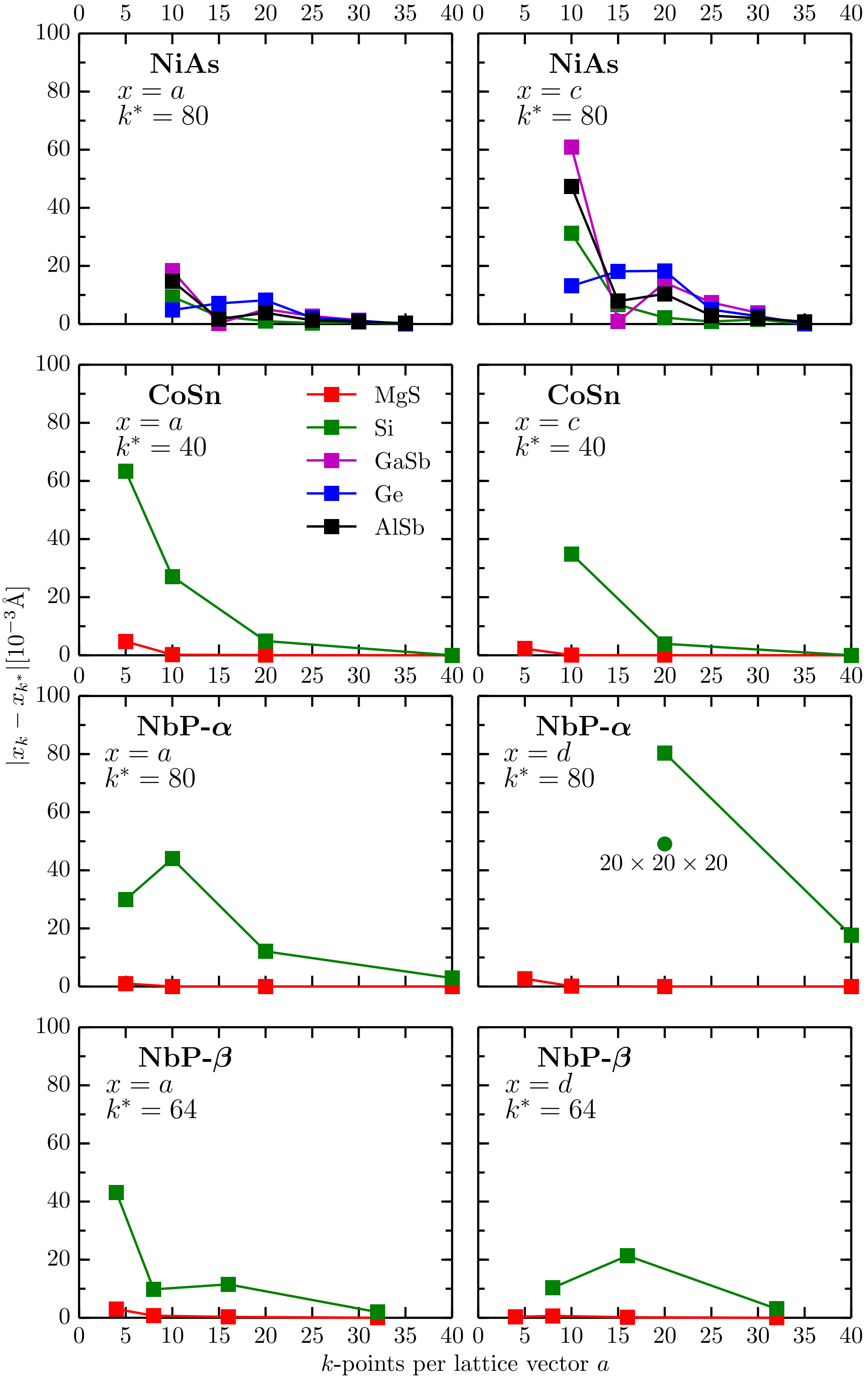

Figure C.6: k-grid convergence test for lattice constant a and c (d) of the non-cubic systems. (5-8)-point BM-fits with a 2%-range are used.

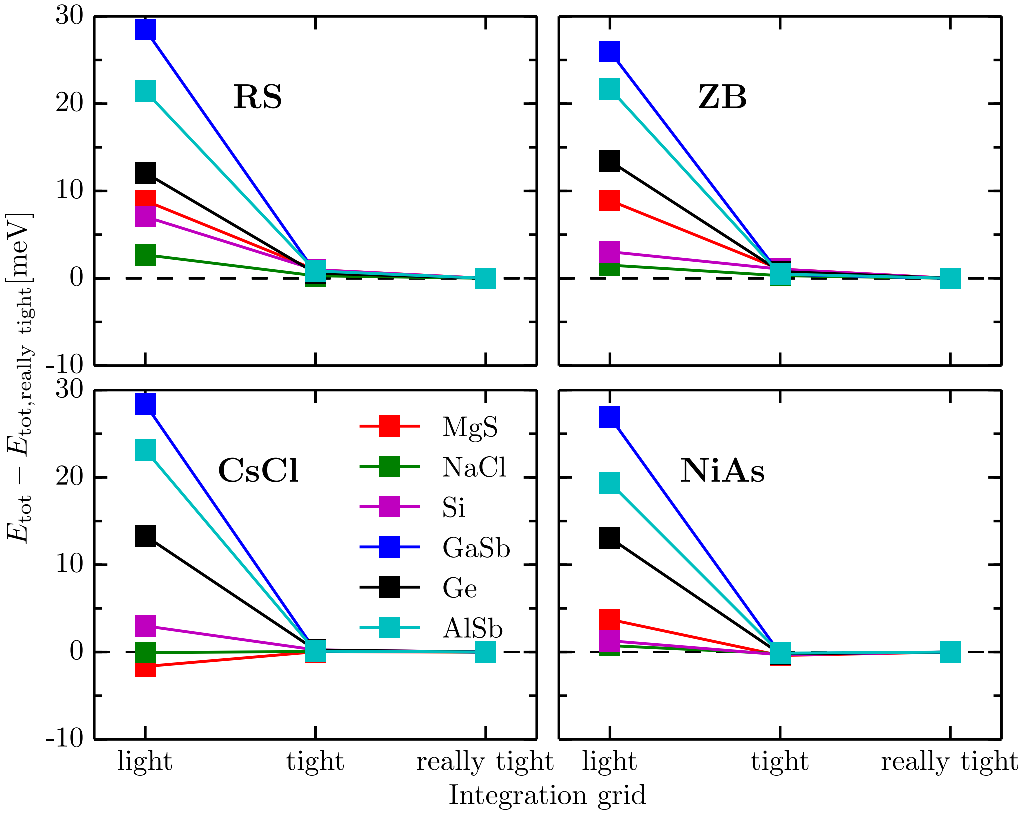

Figure C.7: Integration grid convergence test for total energies. (5-8)-point BM-fits with a 2%-range are used.

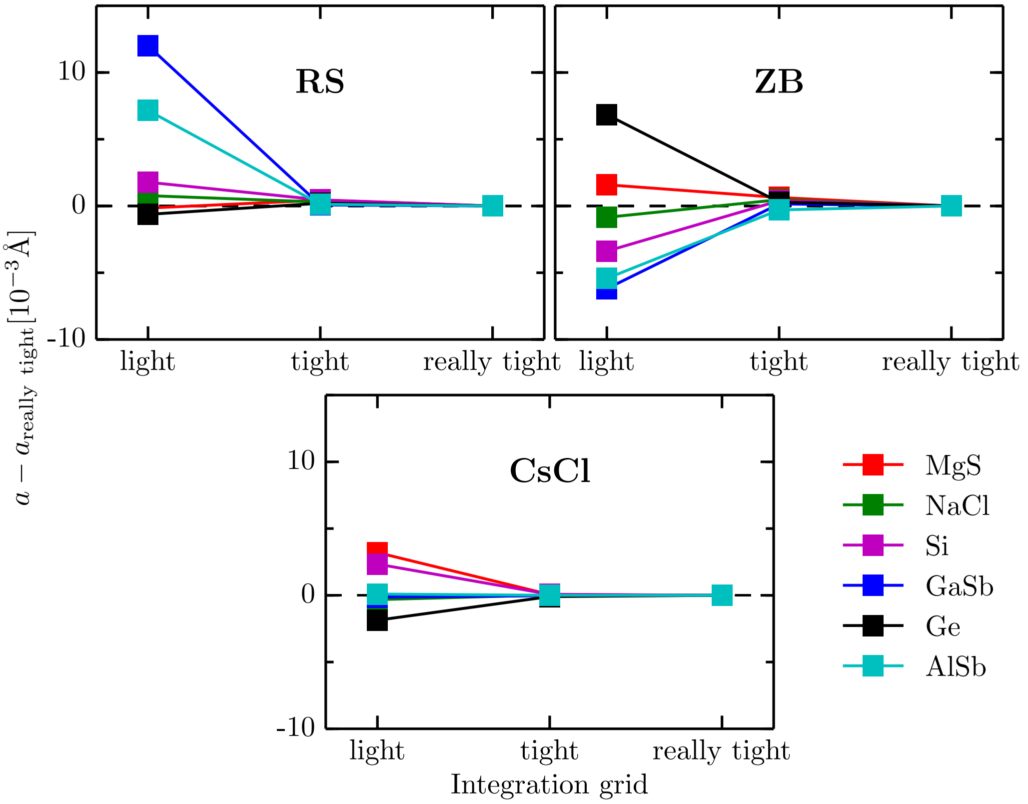

(a) a of the cubic systems. 5-point BM-fits with a 2%-range are used.

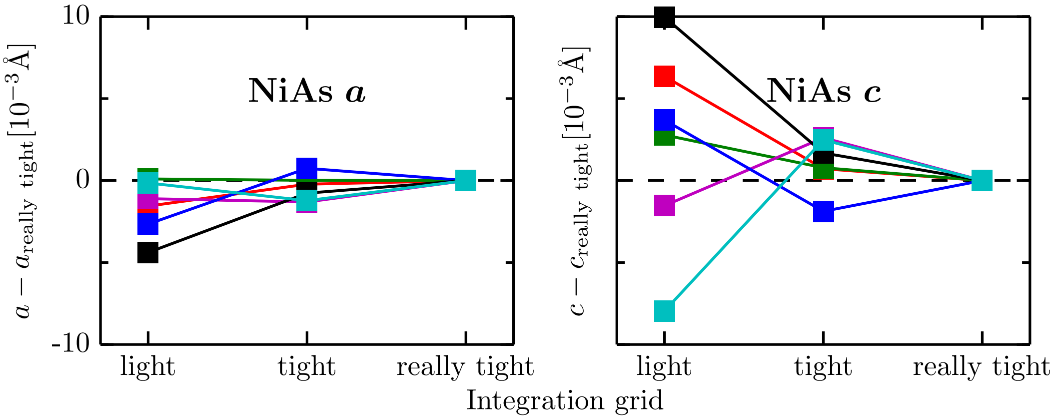

(b) a and c of the NiAs structure. 8-point BM-fits with a 2%-range are used.

Figure C.8: Convergence of the lattice parameters with respect to the integration grids. (5-8)-point BM-fits with a 2%-range are used.

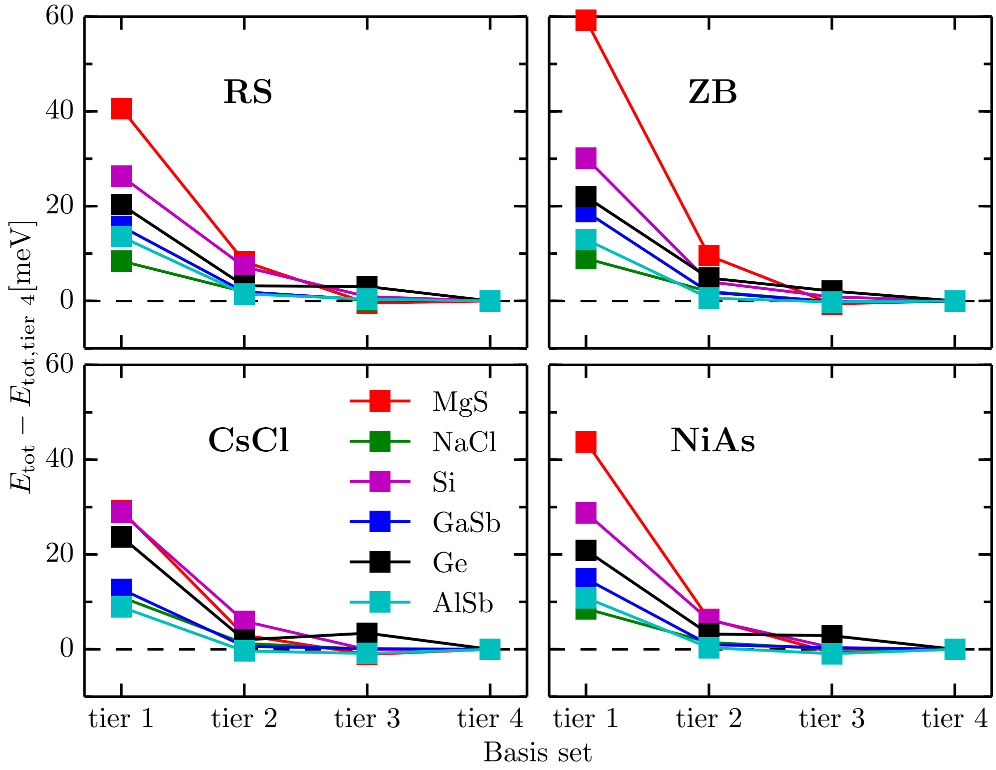

Figure C.9: Basis set convergence test for total energies. The total energies are obtained from (5-8)-point BM-fits with a 2%-range.

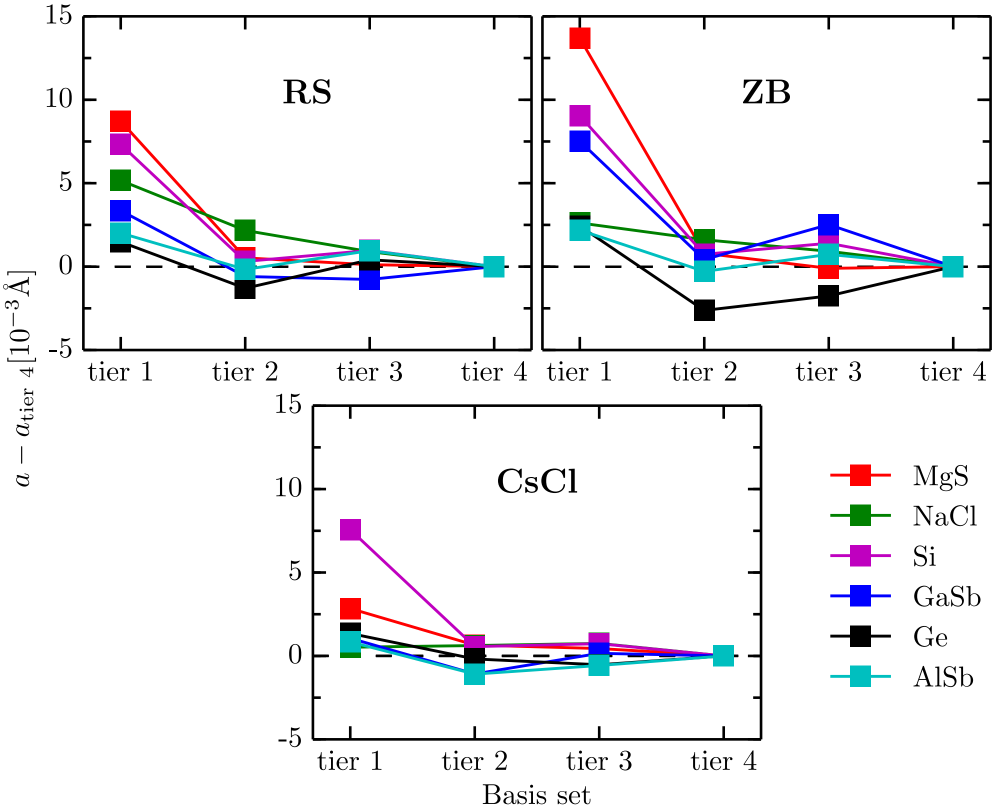

(a) a of the cubic systems. 5-point BM-fits with a 2%-range are used.

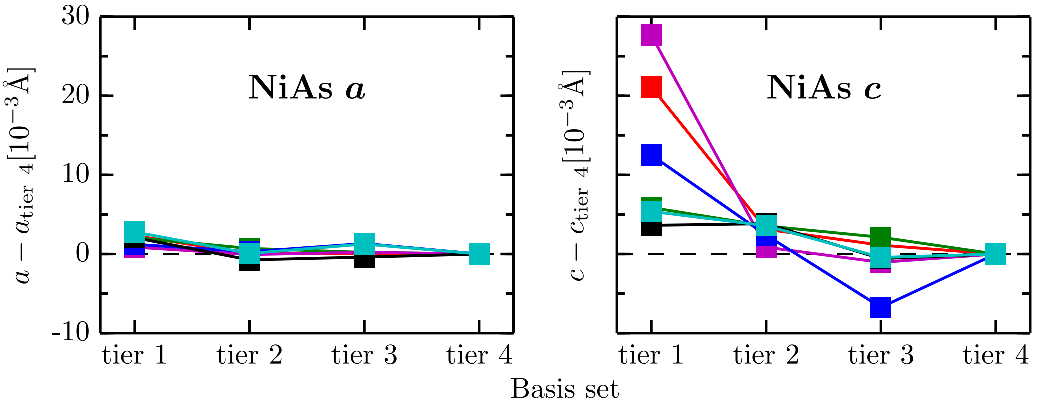

(b) a and c of the NiAs structure. 8-point BM-fits with a 2%-range are used.

Figure C.10: Convergence of the lattice parameters with respect to the basis set.

List of Figures

List of Tables

Bibliography

[1] L. M. Ghiringhelli, J. Vybiral 2 , E. Ahmetcik 1 , R. Ouyang 1 , S. V. Levchenko 1 , C. Draxl 3 , M. Scheffler, work in preparation

[2] R. Ouyang, E. Ahmetcik, L. M. Ghiringhelli, and M. Scheffler, work in preparation

[3] R. M. Martin, Electronic Structure Basic Theory and Practical Methods, Cambridge University Press, Cambridge (2010).

[4] P. Hohenberg and W. Kohn. Phys. Rev. 136, B864 (1964).

[5] Yan Alexander Wang, Niranjan Govind, and Emily A. Carter Phys. Rev. B 60, 16350 (1999).

[6] W. Kohn and L. J. Sham, Phys. Rev. 140, A1133 (1965).

[7] P. J. Perdew, et al., Phys. Rev. Lett, 77 ,18 (1996).

[8] P. J. Perdew, et al., Phys. Rev. Lett, 100 ,136407 (2008).

[9] V. Blum, et al., Comput. Phys. Commun. 180, 2175-2196 (2009).

[10] L. M. Ghiringhelli, J. Vybiral, S. V. Levchenko, C. Draxl and M. Scheffler, Phys. Rev. Lett. 114, 105503, 10 (2015).

[11] E. Mooser and W. B. Pearson, Acta Cryst. 12, 1015-1022 (1959).

[12] The NoMaD (Novel Materials Discovery) repository contains full input and output files of calculations in materials science, http://nomad-repository.eu.

[13] J. C. Phillips and J. A. Van Vechten, Phys. Rev. Lett. 22, 705 (1969).

[14] J. A. Van Vechten, Phys. Rev. 182, 891 (1969).

[15] J. C.Phillips, Rev. Mod. Phys. 42, 317-356 (1970).

[16] J. St. John and A. N. Bloch, Phys. Rev. Lett. 33, 1095-1098 (1974).

[17] P. Brand and J. Briest Z. Anorg. Allg. Chem. 337 (1965) 200-204.

[18] S. Okada and T. Atoda , J. Solid State Chem. 68 (1987) 61-67.

[19] M. Mehl, The AFLOW Library of Crystallographic Prototypes.

[20] D. Pettifor, Bonding and Structure of Molecules and Solids, Calendron Press, Oxford (1995).

[21] D. M. Ceperley and B. J. Alder. Phys. Rev. Lett., 45:566, 1980.

[22] J. P. Perdew and Y. Wang. Phys. Rev. B, 45:13244, 1992.

[23] E. van Lenthe, E. J. Baerends, and J. G. Snijders. J. Chem. Phys., 101:9783, 1994.

[24] U. Fayyad, G. Piatetsky-Shapiro, and P. Smyth, AI magazine 17, 37 (1996)

[25] B. Goldsmith, M. Boley, L. M. Ghiringhelli, and Scheffler, in preparation

[26] R. Tibshirani, J. R. Statist. Soc. B 58, 267 (1996)

[27] J. Friedman, T. Hastie, R. Tibshirani, J. Stat. Softw., 33, 1 (2010).

[28] S. Arora and B. Barak, Computational Complexity: A Modern Approach, University Press, Cambridge, 2009

[29] J. Fan and J. Lv, J. R. Statist. Soc. B 70, 849 (2008)

[30] A. Cohen et al., Compressed sensing and best k-term approximation, J. Am. Math. Soc. 22 211 (2009)